Chemotactic Response Models for Motile Bacteria

Virginia Eirini Kilikian

May 2017

This dissertation by Virginia Eirini Kilikian is accepted in its present form by the Division of Applied Mathematics as satisfying the dissertation requirement for the degree of Doctor of Philosophy.

Date	Martin R. Maxey, Advisor

Recommended to the Graduate Council

Date	Björn Sandstede, Reader
Date	Anastasios Matzavinos, Reader

Virginia Eirini Kilikian received a BSc on Applied Mathematics from the University of Crete in 2008 and an interdisciplinary MSc entitled "Mathematics and its applications" from the Pure and Applied Mathematics Departments of the same university in 2011. Her love for mathematics and ambition for their application on real-world problems led her to pursue a doctoral degree in Brown University.

In the first two years, she had the opportunity to focus on traditional numerical methods to solve physical problems but also got a glimpse of statistical methods and bioinformatics.

During her years as a graduate student, she also discovered the rewarding and fulfilling experience of teaching and involved herself into teaching or mentoring positions whenever they appeared. After serving as a teaching assistant for three years, she co-taught an introductory differential equation course in Summer 2015 that earned the first prize Reginald Archambault award for Summer Session education.

In a search for full-responsibility teaching roles, she applied for the Deans' Faculty Fellowship for the academic year 2016-17. As a Deans' Faculty Fellow, she is expected to teach her own introductory course on Scientific Computing in Spring 2017. While completing this dissertation, she has also been planning, scheduling and designing the course in collaboration with previous instructors and other faculty in the Division of Applied Mathematics.

I have been working on the topic of this thesis for almost four years, but the final result wouldn't have been possible without the academic, emotional and material support I received through various sources.

First and foremost, I want to thank my academic advisor, Professor Martin Maxey, for trusting me in carrying out this project and guiding me through unknown territories. He has taught me to look at mathematical models with a critical eye and to approach a problem in several ways. I'm hoping that my mentoring style will follow his example.

I am also grateful to the Applied Mathematics community at Brown University, especially the staff and graduate students. I feel blessed for being part of such a welcoming and warm family since day one. The Division has also been open to creating teaching opportunities for its students, without which I wouldn't have collected valuable and life-changing experience in teaching.

Furthermore, I appreciate all the people and activities that made me feel at home in Providence. My Greek friends: Dimitra, Sotiris, Odysseas, Martha, Vaios; my fellow graduate students - too many to list here - for years of navigation in Graduate School and important parts of every-day life; Stavroula and the Greek dancing group for taking me to my happy place once a week.

Last, but definitely not least, I extend my thanks to my family in Greece, who wholeheartedly supported my decision to pursue a doctoral degree: my father, Panagiotis, my mother, Sophia, my brother, Alexandros, and my sisters, Renia and Christina. I also undoubtedly owe a large part of my accomplishments to my husband and sanity-keeper, Panos, for his support, encouragement and down-to-earth advice. And, of course, to our daughter, Christina, for boosting my motivation this past year and the effect she had on my own self-definition.

Contents

List of Tables

List of Figures

Chapter 1

Introduction

Chemotaxis is a composite word of the prefix chemo- (for chemical) and taxis (Greek word for marching), coined to describe the biased swimming patterns of bacteria and other biological bodies, in response to extracellular stimuli. Even though we focus on mathematical models for bacterial chemotaxis, similar behaviors are present in neutrophils, sperm and metastasizing cancer cells [22].

Bacteria are among the earliest lifeforms and have evolved over time to occupy and exploit environmental niches, where they can thrive. Many bacteria, such as *Escherichia coli* (E. coli), have a motile phase where they are able to swim in a liquid medium propelled by one or more spiral shaped flagella that spin driven by rotary motors embedded in the cell membrane. A review of the swimming mechanics of microorganisms, including E. coli, is given in [34]. The physical features and anatomy of E. coli are described in a brief summary in [9]. E. coli is a unicellular, rod-shaped bacterium, about $2\mu m$ long and $0.3 - 1\mu m$ in diameter. Around the main body, several spiral shaped protein filaments (flagella) about $10\mu m$ long are attached on the periplasmic membrane to rotary motors that control the direction of rotation of the flagella : clockwise (CW) or counter-clockwise (CCW). Forward swimming (run) comes from CCW rotation, where the flagella bundle together to form a single effective spiral flagellum that propels the cell, head first. In the reverse CW mode, the flagella unbundle and the cell wiggles in place (tumble) before swimming in a new direction as the cell resumes a CCW mode. For an illustration, refer to Figure 1.1. The swim speed of a cell varies somewhat with the fluid medium and temperature but is often about $15 - 25\mu m/s$ and a run may persist for $1 - 2s$. Without any stimulus, the cells migrate diffusively and are characterized by a random motility coefficient.

Cells grow and divide on a time scale of $20 - 30$ minutes. For this, they require an energy source for metabolism and aminoacids to build the proteins and cell structure needed for cell

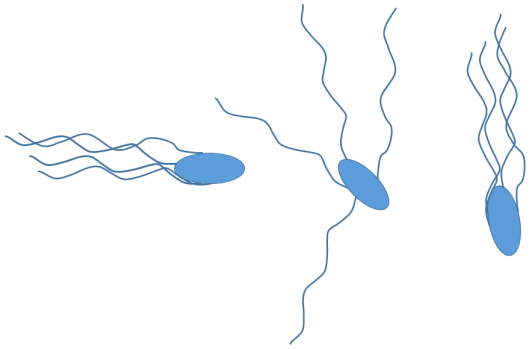

Figure 1.1: Sketch of an E. coli cell running (left), tumbling (middle) and beginning a new run (right).

growth. The switch between CCW and forward swimming (run) to CW and tumbling in place (tumble) is in turn controlled by internal biochemical processes, involving signals between proteins and the cell's organelles : the chemoreceptors and motors. In a sense, the chemoreceptors on the cell surface act to detect changes in the concentration of attractants or repellents, similar in function to a human nose. The cells have evolved a strategy for detecting gradients of attractants or repellents that allow them to search for beneficial environments efficiently. They are too small to directly sense a spatial gradient against the effect of thermal fluctuations and at the low concentrations that are often in the μM range for the attractants. Instead, they are found to detect changes in concentration over time and thus effectively the changes over the distance of a forward run. This can then produce a net drift velocity (or chemotactic drift) of the cell towards the source of an attractant.

Other bacterial species that perform chemotaxis are the marine bacterium Vibrio alginolyticus and Caulobacter crescentus, typically found in fresh water. These both have a single flagellum, that rotates either CW or CCW, resulting in a different pattern of swimming, known as "run-reverse-flick". In general, these bacteria swim faster than E. coli and have shown the ability to localize around a source of attractants [56].

The first experiments on E. coli, that have been points of reference for subsequent studies, were conducted independently by Julius Adler [1, 2] and Howard Berg [10, 13, 49]. Adler examined cells migrating up a capillary tube or spreading in waves on an agar plate with various aminoacids, such as aspartate, seeded in the medium. Berg experimented with modified cell strains, where certain components of the chemotactic response pathway were turned on or off. In 1986, Berg et al. measured the duration of the run and tumble intervals of tethered as well as free-swimming cells and documented their adaptation, the long-term response that resets the receptors at a new equilibrium, when subject to a persistent stimulus [49].

Following the publication of these observations, the first mathematical models emerged: initially, Keller-Segel formulated a phenomenological PDE model for the cell density [32], and

later Segel [50] suggested a simple response model for the chemoreceptors of cells moving up or down a chemical gradient. Later on, the first random walk models were proposed, based on the past experiments by Berg [5,48]. Recently, more sophisticated empirical models for the response of a single cell have been designed [14,17,37,68], based on the measurements in [49].

However, as more of the internal structure and signaling pathways of bacteria became better known, there has been a shift to a systems biology approach. First, Fluorescence Resonance Energy Transfer (FRET) measurements have enabled experimentalists to isolate chemical interactions and their individual elements, and examine them as separate parts of the signaling pathway. Also, the advancements in tracking equipment have offered high resolution images of cell swimming, motor characteristics and interactions between cells or cells and surfaces. A now standard experimental technique was first developed by Roman Stocker, using a microchannel to generate controlled attractant gradients and measure chemotaxis, either through the cell density profile or by cell tracking [3].

These developments gave rise to biochemical pathway models, modeling the internal processes that trigger a cell's macroscopic response. FRET imaging combined with free-swimming or tethered cells experiments provide a more detailed understanding of the internal processes [7,12,19]. Figure 1.2 shows the mostly-characterized chemosensory system of E. coli: the binding of ligand (chemoattractant) to the methyl accepting receptor (MCP) in the periplasm suppresses the receptor activity $a(t)$. The receptor is considered to include the tightly bound enzymes CheW and CheA. In its active state, CheA can auto-phosphorylate to form CheA-P. CheA-P transfers the phosphor group to the freely diffusing CheY protein to form CheY-P. In turn, CheY-P binds to the FliM motor proteins and promotes switching, which for E. coli leads to a tumble event. The binding of an attractant ligand thus leads to a lower rate of switching and longer run times. Methylation, $m(t)$, promotes receptor activity and counters the effect of ligand binding. CheR acts continuously to raise the methylation of the receptor but may act preferentially on inactive receptors. CheB-P is also formed by CheA-P and this acts to suppress the methylation level and may act preferentially on active receptors. This generates a feedback loop to maintain the receptor at an equilibrium level of activity. The effect of ligand binding on CheA is relatively fast, about $0.01s$, while methylation is much slower. The enzyme CheZ will act to dephosphorylate CheY-P before it acts on the motor. Lastly, CheY may have varying levels of auto-phosphorylation or auto-dephophorylation.

This thesis is written in the following chapters: Chapter 2 offers an overview of existing models and how their approaches differ. First, we mention the PDE models, mainly the Keller-Segel model. Then, we describe the reduced models, which model the individual cell response according to the experimental data in [49]. These are the linearized, empirical models that link

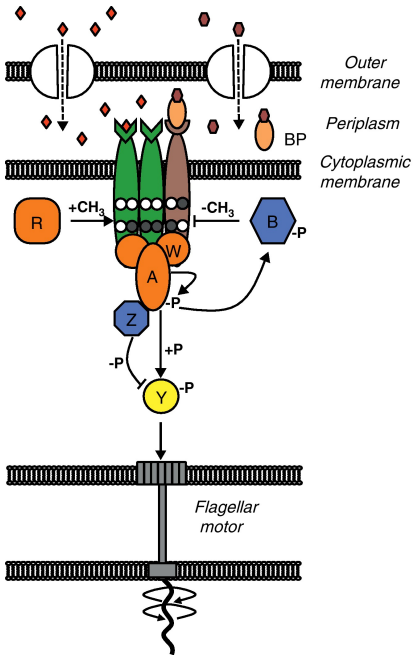

Figure 1.2: The signaling pathway in E. Coli. Ligand molecules pass through the outer membrane and bind to chemoreceptors in the periplasm. The brown and green structures represent the Tar and Tsr methyl-accepting chemotaxis protein (MCP) respectively that span the cytoplasmic membrane. Each kind of receptor binds with different kind of molecules eg. Tar receptors bind with aspartate and Tsr receptors bind with serine. CheW and kinase CheA are localized and clustered with the receptors. CheA auto-phosphorylates and its phosphor group is then released and binds to the freely diffusing CheY. CheY-P diffuses in the cytoplasm and reaches the flagellar motors, inducing a switch. CheY-P can lose its phosphor group by auto-dephosphorylation or by action of CheZ. Proteins CheR and CheB regulate the methylation level of the receptors, countering the loss of CheA activity on a slower timescale. Reproduced from [55], with permission.

changes in the surrounding attractant concentration to the mean run time of the cell. Details are given of the model by Celani et al. [14] and Xue et al. [68], as we use them for our simulations. A summary is given in Table 2.1 for two other models primarily chosen for E. coli. In Chapter 3, we focus on the kernel-type reduced models given in Chapter 2 and compare their parameters in some benchmark cases: pulse, step change and ramp stimuli. We introduce the $F(Q)$ model for the run time modulation and add other features, such as the reorientation bias, finite tumble time and Brownian rotation. We implement Monte Carlo simulations to test the model assumptions of PDEs and highlight features that are beyond the weak response asymptotics. In Chapter 4, we test the performance of pathways models that aim to capture a more detailed chemotactic response. We adopt common assumptions about the linkage of activity of the receptors to the concentration of CheY-P that binds to the FliM proteins in the motors and induces reverse rotation. In Chapter 5, we apply a kernel-type model to the Caulobacter and its "run-reverse-flick" behavior, assuming a fixed mean reverse run time. We end with conclusions and future directions at Chapter 6.

Chapter 2

Overview of Existing Models

Chemotactic behaviors have been examined by a range of scientists, including biologists, mathematicians and engineers. Even though Escherichia coli (E. coli) is the most extensively studied bacterial species [1–3, 10, 11, 13, 14, 17, 19], single-flagellum bacteria, like *Vibrio alginolyticus*, *Caulobacter crescentus* and *Rhodobacter sphaeroides*, have been appearing in recent research, in [6], [36, 43, 45] and [24] respectively. The development of more accurate and sophisticated tracking equipment has made it possible to observe more details in experiments and include more features in the related mathematical models.

Chemotactic processes can be viewed in three levels of description :

1. on a population level, with a PDE model for the density of cells $b(x,t)$. Keller and Segel proposed the first PDE model in 1971, based on phenomenological observations [32]. Variations of the Keller-Segel model have emerged since then [27].

2. on individual cell behavior level, with reduced models of internal pathways [3, 14, 37, 68]. Typically, there is a short-term response to a change in concentration of chemoattractants (excitation) and a long-term response to an invariable level of chemoattractants (adaptation). These models are semi-empirical and refer back to the findings in [49] to represent the overall response in an aggregated way. Homogenization and other asymptotic methods can link the individual cell models to a Keller-Segel-type PDE.

3. on internal dynamics and cell biochemistry level, with diffusion models and chemical pathways that trigger changes in motor rotation [59]. Such models describe the sequence of processes from ligand binding on the periplasmic chemoreceptors to phosphorylation of Che- proteins and methylation of receptors. They range from reduced mean-field models to detailed mean-field models and Ising models.

2.1 The PDE Models

In the 60's, Adler systematically experimented with E. Coli to figure out its sensing mechanism and characterize its chemotactic behavior. He tested how the cells respond to different kinds of energy sources by filling capillary tubes with a liquid medium rich in 20 aminoacids, inserting E. Coli cells on one end and sealing both ends with agar (see Figure 2.1). He observed that the cells moved towards the other end of the tube in two separate bands: the first one consumed almost all of the oxygen; the second one, in the absence of oxygen, metabolized serine, the only aminoacid that can be consumed anaerobically. This group behavior of a population of bacteria motivated the formulation of PDE models.

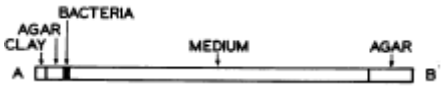

Figure 2.1: Figure 1 in [2] sketching the experimental setup in a capillary tube. The middle of the tube is filled by a solution containing aminoacids and bacteria are injected in one end and both ends are insulated with agar. The bacterial population is seen to move in traveling bands over time from end A to end B.

Historically, the most common point of reference for PDE models of bacterial chemotaxis was suggested by Keller and Segel in 1971 [32]. The description is in terms of bacterial concentration (or density) and the chemotactic velocity of the bulk of the population swimming up a nutrient gradient. The model takes into account the diffusion of bacterial cells and nutrients, the chemotactic drift, cell population growth and nutrient consumption. If $b(\vec{x},t)$ and $c(\vec{x},t)$ stand for the concentration of bacteria and nutrients respectively at location $\vec{x}$ and time t, then the Keller-Segel model can be written as the system of two partial differential equations:

$$\begin{cases} \dfrac{\partial b}{\partial t} = \underbrace{\mu\nabla^2 b}_{\text{diffusion of bacteria}} \underbrace{-\nabla\cdot(\chi b\nabla c)}_{\text{chemotactic flux}} \underbrace{+\alpha b}_{\text{population growth}} \\ \dfrac{\partial c}{\partial t} = \underbrace{\nu\nabla^2 c}_{\text{diffusion of nutrients}} \underbrace{-\beta b}_{\text{nutrient consumption}} \end{cases} \tag{2.1}$$

where μ and ν are the random motility coefficients of bacteria and nutrients respectively, χ the chemotactic coefficient, α the cell growth rate and β the nutrient consumption rate. The drift velocity is defined as

$$v_{\text{drift}} = \chi\nabla c \tag{2.2}$$

and characterizes the effect of the presence of a gradient of attractants to bacterial swimming.

Models of the Keller-Segel type have been derived by perturbing the cell balance equation proposed by Alt [5] or Segel [50], which express cell density with a differential-integral system. Chen, Ford and Cummings also derived formulas for the motility coefficient and drift velocity

as functions of individual cell properties [15], as discussed further in Section 3.4.4.

More models of the Keller-Segel type have emerged to model patterns in other settings, like slime mold motility, neutrophil response to infection, tumor growth and larger-scale problems in spatial ecology [27].

2.2 The Reduced Models

Moving on from band formation in Adler's experiments, improvement of imaging techniques in the 70's allowed for tracking of individual cells. Howard Berg conducted a series of experiments with tethered and free-swimming E. Coli cells and characterized their response to different types of attractants. His work became an important milestone in chemotaxis research and motivated a new style of mathematical models focusing on individual rather than collective behavior.

The 1972 paper [10] measured the reorientation angles, the difference in direction of swimming between two consecutive runs. In the same study, empirical distributions for the duration of runs (run time) and duration of tumbles (tumble time) are presented. They both had an exponential form, with the tumble time having a lower mean. This led to a common practice of modeling chemotaxis as a Poisson process. The data was obtained by counting how long a tethered cell was spinning clockwise or counter-clockwise. When all flagella of an E. Coli cell rotate counter-clockwise (CCW), the cell swims forward; when one or some of the flagella spin clockwise (CW), the cell stays in place tumbling briefly before running to a new direction. Pinning the cells down and recording their rotation made it possible to determine the duration they stayed in running or tumbling states. Two years later, the same authors [13] proposed a model for the change in run time, modeling the chemotactic effect as an exponential process. Later work in 1986 [49], fitted experimental data from tethered cells (see Figure 2.2) to what would later become a kernel representation of the chemotactic effect and set the stage for a set of new models, aiming to derive estimates for the chemotactic drift and random motility, starting from the individual response [3, 14, 17, 29, 30, 37, 68].

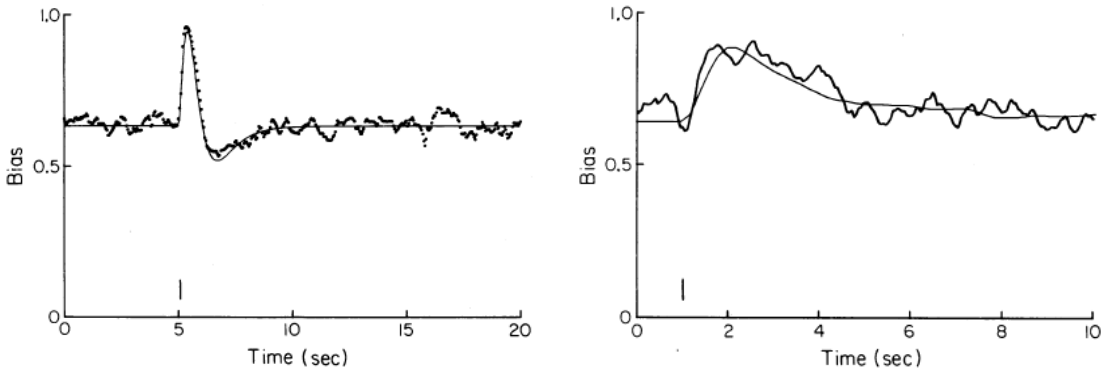

Figure 2.2: Figures 1 and 2 in [49]. Responses to attractants by tethered cells. The solid lines are fitted to the data. The dots represent the empirical probability of a tethered cell "running" (spinning CCW) after exposure to: a pulse of chemoattractant applied at the time marked by the tick at $5s$ (left); a step-change of chemoattractant applied at the time marked by the tick at $1s$ (right).

Thus, a new style of models emerged [14, 37, 68] to describe chemotaxis in terms of the mean tumble rate σ or mean run time $\tau = \dfrac{1}{\sigma}$ that are modified as a cell swims in an environment of a non-uniform distribution of chemoattractants or chemorepellents. Each model estimates a bias term Q that represents the proportional increase ($Q > 0$) or decrease ($Q < 0$) of the mean run time. Relevant range of values of Q is $|Q| < 1$. Most models assume a weak response to changes in the gradient of nutrients, where $|Q| < 0.3$. Each of these models can be put in the form

$$\tau = \tau_0 F(Q) \tag{2.3}$$

where τ_0 is the baseline mean run time, i.e. in the absence of changes in the level of attractants, and $F(Q)$ is an increasing, non-negative function of Q. Further details on response functions follow in Section 3.2.2.

There is a number of options for defining Q. This *bias* term represents the memory of a cell as it performs temporal comparisons and adapts its mean run time accordingly. Mathematical models developed in [14], [17], [37] and [68] all use a kernel representation of Q :

$$Q(t) = \int_{-\infty}^{t} K(t-s)C(s)\,\mathrm{d}s \tag{2.4}$$

where $C(s)$ is the concentration experienced by the cell at time s and $K(t)$ is a two-lobe, zero-integral function. These properties of $K(t)$ are consistent with the experimental results reported in [49]. The kernel function $K(t)$ can be viewed as the response of initial excitation (positive lobe) and eventual adaptation (zero integral) of a cell when exposed to a stimulus δ_0. The zero-integral property ensures exact adaptation, resetting the cell to a neutral response in case of a persistent constant level of attractants. Several models with a memory kernel structure

have been developed, as listed in Table 2.1. Figure 2.3 shows the shape of kernels in the reduced models listed. The definition of the kernel function has to agree in shape with the experimentally obtained response to a pulse input by [49], pictured on the left of Figure 2.2. On the right-hand side of Figure 2.2 is the response to a step change, another basic test examined in [49]. When cells were abruptly exposed to a constant level of attractant, they had an immediate response, corresponding to the peak shortly after the step change, that gradually returns to the default levels. Note that compared to the short initial response time ($\sim 0.5s$), the adaptation process takes longer ($\sim 3s$). In Figure 2.4, are the corresponding responses to a step change for the models listed in Table 2.1.

model by	kernel function $K(t)$
Celani [14]	$\beta_1 \ell e^{-\ell t}\left[\ell t - \frac{1}{2}(\ell t)^2\right]$
Clark & Grant [17]	$\alpha \ell N e^{-\ell t}\left[1 - \frac{1}{2}\ell t - \frac{1}{4}(\ell t)^2\right]$
Locsei [37]	$\frac{2\varepsilon \ell^2}{3} e^{-\ell t}\left[1 - \frac{1}{2}\ell t - \frac{1}{4}(\ell t)^2\right]$
Xue & Othmer [68]	$\frac{b\tau_0}{t_e(t_a - t_e)}\left[t_a e^{-t/t_e} - t_e e^{-t/t_a}\right]$

Table 2.1: The kernel functions used for each model in the corresponding references. β_1, ℓ, α, N, ε, b, t_e, t_a are all parameters of the kernel model in which they appear. ℓ^{-1} and t_a represent timescales for adaptation, while τ_0 is the mean run time without chemotaxis.

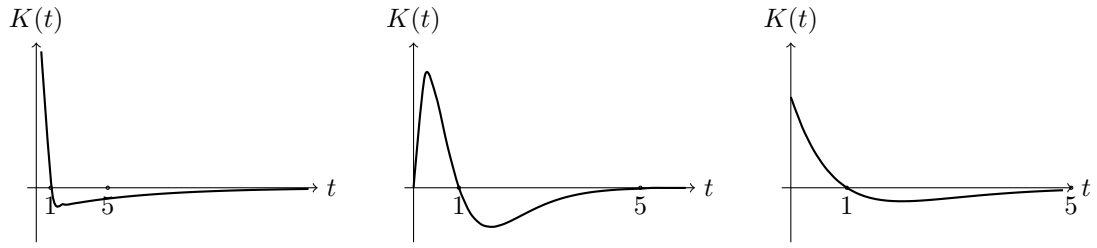

Figure 2.3: Shape of kernel functions for the models listed in Table 2.1. The kernel function is also the response to a pulse of attractants experienced at time $t = 0$, $C(s) = \delta_0(s)$. From left to right: Xue & Othmer; Celani & Vergassola; Clark & Grant, Locsei.

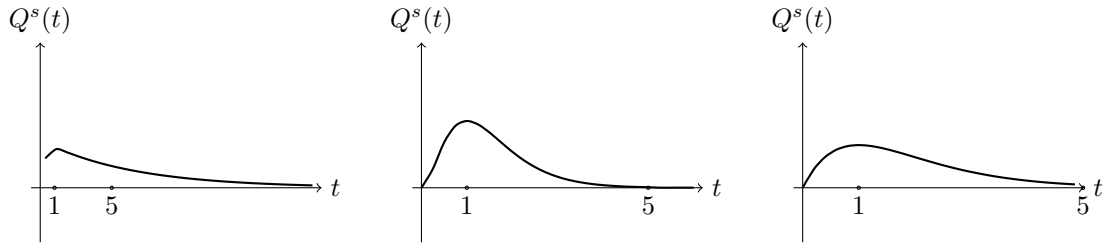

Figure 2.4: Shape of response to a step change applied at time $t = 0$, $C(s) = H(s)$, where H is the Heaviside function, for the models listed in Table 2.1. From left to right: Xue & Othmer; Celani & Vergassola; Clark & Grant, Locsei.

In Chapter 3, we discuss the details of comparing outcomes of two of the models in Table 2.1 that we use for our simulations. In particular, we use the three examples of a pulse, step and linearly increasing (or decreasing) attractant concentration $C(t)$ to calibrate and match each model's parameters. The third test case, where C is a steadily increasing (or decreasing) function corresponds to the scenario of 1D motion directed up (or down) a specific concentration gradient. Figure 2.5 shows the respective response given by the kernel models in Table 2.1.

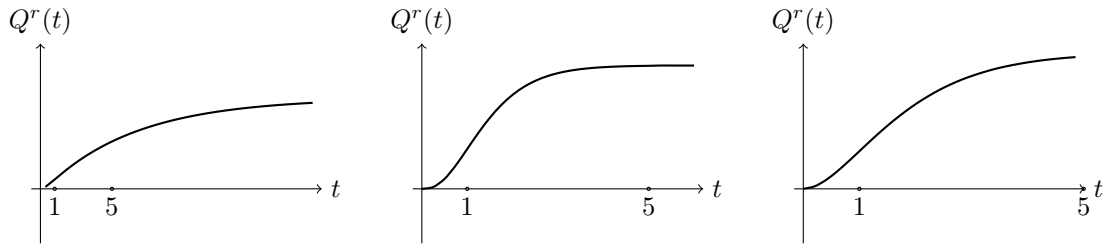

Figure 2.5: Shape of response to a linear concentration over time $C(s) = s$ for the models listed in Table 2.1. From left to right: Xue & Othmer; Celani & Vergassola; Clark & Grant, Locsei.

2.2.1 Two Reduced Models

Here, we describe two of the reduced models as presented in [14] and [68]. We keep the same notation as in the original papers.

Celani-Vergassola [14] The starting point of this model is the response to a pulse, as reported in [49]. The authors assume that the kernel is a sum of exponentials and choose the coefficients so that the chemotactic drift is maximized. The kernel is assumed to be in the form

$$K(t) = \lambda e^{-\lambda t} \sum_{k=1}^{k_M} \beta_k \left(\lambda t\right)^k, \; t \geq 0; \qquad K(t) = 0, \; t < 0 \tag{2.5}$$

where the sum is over a finite number of terms k_M and λ, β_k are parameters. The bias

term is then

$$Q(t) = \sum_{k=1}^{k_M} \lambda^{k+1} \beta_k m_k(t) \tag{2.6}$$

where $m_k(t)$ satisfy the system of equations

$$\frac{\mathrm{d}m_k}{\mathrm{d}t} = -\lambda m_k + f_k, \text{ where } f_k = k m_{k-1},\ k \geq 1; \qquad f_0 = C(t),\ k = 0 \tag{2.7}$$

This is a linear system of ODEs that can be solved analytically or numerically. More details on implementation can be found in Chapter 3. This model doesn't take saturation into account, meaning that the chemoreceptors are assumed to respond to any level of attractant, which is not always realistic. Normally, after a certain threshold, more attractants do not have an additional effect on the response, due to the finite number of binding sites on the receptors. However, this should not be an issue for moderate concentrations, which is the case for our simulations. Celani and Vergassola also study the performance of the model for increasing number of terms in the sum, concluding that there is not much gain by including more than 2. When $k_M = 2$, a necessary condition to satisfy the zero-integral property of the kernel $K(t)$, is to set $\beta_2 = -\beta_1/2$.

The authors also provide a derivation of a Keller-Segel PDE for the bacterial density and derive asymptotic estimates for the chemotactic drift and random motility in the presence or absence of Brownian rotation in a uniform concentration gradient $\nabla C = (c_1, 0)$.

- If $D_r = 0$ (no Brownian rotation), then the chemotactic coefficient in [14] is

$$\frac{\chi_C c_1}{v_s^2} = \frac{\beta_1 c_1}{d} \frac{\lambda^2 \tau_0^3}{\left(\lambda\tau_0 + 1 - \langle \cos\Phi \rangle\right)^3} \tag{2.8}$$

- If $D_r \neq 0$ (non-zero Brownian rotation), then the chemotactic coefficient in [14] is

$$\frac{\chi_C c_1}{v_s^2} = \frac{\beta_1 c_1}{d} \frac{1 - \langle \cos\Phi \rangle}{D_r(d-1)\tau_0 + 1 - \langle \cos\Phi \rangle} \frac{\lambda^2 \tau_0^3}{\left(\lambda\tau_0 + D_r(d-1)\tau_0 + 1 - \langle \cos\Phi \rangle\right)^3} \tag{2.9}$$

In both formulae, $\langle \cos\Phi \rangle$ is the mean cosine of the reorientation angle, the difference in direction between two consecutive runs, d is the spatial dimension and v_s is the swimming speed. The random motility coefficient μ remains the same as in the non-chemotactic case.

Xue-Othmer [68] The authors adopt a minimal model for the excitation and adaptation phases of the response to a pulse of chemoattractants. The corresponding system of ODEs

for the internal variables $y_1(t), y_2(t)$ is

$$\begin{cases} \dfrac{\mathrm{d}y_1}{\mathrm{d}t} &= \dfrac{G(C) - (y_1 + y_2)}{t_e} \\ \\ \dfrac{\mathrm{d}y_2}{\mathrm{d}t} &= \dfrac{G(C) - y_2}{t_a} \end{cases} \tag{2.10}$$

and

$$Q(t) = by_1\tau_0 \tag{2.11}$$

for some proportionality constant b. The two variables y_1 and y_2 aim to model the excitation and adaptation stages of the chemotactic response respectively. Starting from equilibrium, a step change increases y_1 initially. In the long run, $G(C) \sim y_2$ and y_1 is restored to zero. The parameters t_e and t_a set the excitation and adaptation timescale and $t_e < t_a$. This system can be solved analytically and numerically for a given concentration history $C(t)$. The model builds in the receptor saturation effect by setting $G(C) = G_0 \dfrac{C}{K_D + C}$, where K_D is the binding coefficient of ligand to the receptors. More specifically, K_D is the ratio of unbinding and binding rates of ligand (C) to receptor (R) in the Michaelis-Menten kinetics : $K_D = \dfrac{k_-}{k_+}$

$$C + R \underset{k_-}{\overset{k_+}{\rightleftharpoons}} CR \tag{2.12}$$

An alternative of the model sets $t_e = 0$ so that excitation is instantaneous and $C \ll K_D$ to get

$$\begin{cases} y_1 &= C - y_2 \\ \\ \dfrac{\mathrm{d}y_2}{\mathrm{d}t} &= \dfrac{C - y_2}{t_a} \end{cases} \tag{2.13}$$

This model is also coupled with a PDE model, so drift velocity and random motility are also obtainable. The authors do not consider the effect of Brownian rotation, and the chemotactic drift in a uniform gradient $\nabla C = (c_1, 0)$ is given by

$$\frac{\chi_{\mathrm{XO}} c_1}{v_s^2} = \frac{bt_a}{d} \frac{\tau_0^2}{\tau_0 + (1 - \langle \cos\Phi \rangle)\, t_a} \tag{2.14}$$

where $\langle \cos\Phi \rangle$ is the mean cosine of the reorientation angle, d is the spatial dimension and v_s is the swimming speed. Similarly to the first model, the random motility coefficient remains the same as in the non-chemotactic case.

The given asymptotic results for drift velocity ignore the finite duration of tumble events.

The CCW bias of a wild-type E. coli cell, i.e. the fraction of time it spends running, has been measured to be close to 0.7 when it is not performing chemotaxis. If τ_0, τ_t are the mean run time and mean tumble time respectively, then

$$\frac{\tau_0}{\tau_0 + \tau_t} \sim 0.7 \tag{2.15}$$

giving a magnitude of the duration of tumble intervals relative to the mean run time: $\tau_t \sim \frac{3\tau_0}{7}$. The effect of finite tumble times is further investigated in Section 3.4.3. Generally, it is assumed that the distribution an mean value of duration of tumble intervals in unaffected by the presence of attractants.

Both models link Q to the modified mean run time as

$$\frac{1}{\tau} = \frac{1}{\tau_0}(1 - Q)$$

which is one of the standard response models we include in Section 3.2.2.

2.3 The Pathways Models

The advancement in imaging technology has allowed for scientists to look deeper into the cytoplasm and examine the chemical signaling process that controls the response of the rotary motors in more detail [4, 6, 19, 30, 35, 41, 62]. The developments in this kind of mathematical models for chemotaxis are fairly recent and are the subject of current research. As such, it is unclear what the best assumptions in dynamics are but a number of simplified models have been proposed [7, 12, 30, 61, 70].

Chapter 3

Modeling Chemotactic Response of E. Coli

On a macroscopic level, the motion pattern of E. coli is known as "run-and-tumble". A wild-type cell swims in a sequence of straight runs and reorientations in place (tumbles). When moving towards a more favorable environment, the duration of these runs is extended, while, when moving towards toxins or less desirable conditions, the runs are shortened and the cell tumbles more often. The same strategy is also seen in some uni-flagellated bacteria, like *Serratia marcescens* [70].

The discussion in this chapter focuses on cell motion in two dimensions. This allows for directional effects as commonly seen in experiments without the extra complexity of three dimensional motion. The same principles can be extended to three dimensional counterparts in a straightforward way. Besides, the simulations we set up in Matlab are more manageable in 2D, and we are able to explore more conditions.

3.1 Cell Motion Without Chemotaxis

An E. coli cell executes forward runs with CCW rotation of the flagella as viewed from behind, alternated with tumbles in place (CW motor rotation) and reorientation of the cell to swim in a new direction. Refer to Figure 3.1 for a sketch of the change in direction Φ following a tumble event. The reorientation angle, and any possible bias in its value, plays a significant role in a cell's migration capability. Within each run interval, the cell swims at a constant swimming speed v_s. A possible change in swimming speed with chemoattractants - chemokinesis - is not observed, although in a population of cells it is likely that v_s shows some variation between cells.

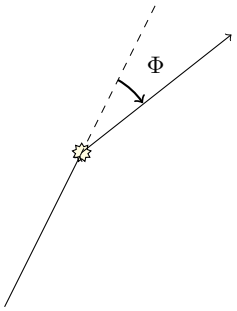

Figure 3.1: A tumble event.

Without chemotaxis, the cell executes a random walk with runs of varying duration τ_r given by a Poisson process. This is consistent with the observed exponential probability density function for the duration of a run [10]. Thus, the probability that a running cell switches to a tumble in the short interval $(t, t+\Delta t]$, is $\dfrac{\Delta t}{\tau_0}$. For a cell that starts a run at time $t = 0$, the probability that it is still in the same run interval at time $t > 0$ is $\exp\left(-t/\tau_0\right)$ and the probability for the run to end at time $t > 0$ is $\dfrac{\Delta t}{\tau_0} \exp\left(-t/\tau_0\right)$. Without chemotaxis, there is no preference in the direction of swimming, so that the mean run time is τ_0 in all directions. With this isotropy, there is no mean drift.

Relative to a fixed set of axes, the velocity components of a cell at time t are

$$(v_x, v_y) = v_s \left(\cos\theta(t), \sin\theta(t)\right) \tag{3.1}$$

where $\theta(t)$ is the polar angle of the cell position at time t. If the change in direction $\theta \leftarrow \theta + \Phi$ at the end of a run is purely random, i.e. $\Phi \sim \mathcal{U}\left[-\pi, \pi\right]$, any correlation with prior velocity is lost after a tumble event. Noting that $\langle v_x \rangle = 0$, the velocity autocorrelation is

$$\langle v_x(t_1) v_x(t_2) \rangle \quad = \quad v_s^2 \left\langle \cos\theta(t_1) \cos\theta(t_2) \right\rangle$$

This calculation is useful in determining the mean square displacement that is linked to the random motility coefficient, as further explained in Section 3.3.

$$\left\langle X^2(t) \right\rangle = \int_0^t \int_0^t \langle v_x(t_1) v_x(t_2) \rangle \, \mathrm{d}t_1 \, \mathrm{d}t_2 \tag{3.2}$$

For statistically stationary processes, the integrated quantity only depends on the time difference $s = t_2 - t_1$ and therefore, $\langle v_x(t_1) v_x(t_2) \rangle = \langle v_x(0) v_x(s) \rangle$. For durations smaller than the mean run time τ_0, the two velocities are on the same direction and $\langle v_x(0) v_x(s) \rangle = \dfrac{1}{2} v_s^2$, since $\left\langle \cos^2\theta \right\rangle = 1/2$ for θ uniform in $(-\pi, \pi]$. Equation (3.2) then gives a quadratic behavior for small t: $\left\langle X^2(t) \right\rangle = \mathcal{O}\left(t^2\right)$. For longer time difference, the autocorrelation drops to zero and $\left\langle X^2(t) \right\rangle \sim 2 D_x t$ [20],

where

$$D_x = \int_0^\infty \langle v_x(0)v_x(s)\rangle \, \mathrm{d}s \tag{3.3}$$

If there is no preference when picking a new direction, there is no correlation of θ between runs. Thus $\langle v_x(0)v_x(s)\rangle = \frac{1}{2}v_s^2 \exp\left(-s/\tau_0\right)$ giving the random motility coefficients in the x and y direction as

$$D_x = D_y = \frac{v_s^2\tau_0}{2} \tag{3.4}$$

It is easy to derive the exponential decay of the velocity autocorrelation when there is no drift ($\langle X(t)\rangle = 0$) by looking at the mean square displacement. We also consider finite tumble times, a factor that some models omit, assuming instantaneous reorientations. In reality however, it has been observed that when cells tumble it takes a little time before they start running again [13]. Tumble times, similar to run times, follow an exponential distribution with a mean τ_t smaller in magnitude to τ_0, estimated to be close to one tenth of a second. Unlike mean run times, the distribution of tumble times remains virtually unchanged by external conditions.

Another important feature of swimming bacteria is Brownian rotation. Bodies moving in a liquid medium are subject to small random reorientations due to collisions with the liquid molecules. For swimming bacterial cells, this effect depends on the shape and size of the cell in question [22]. Effectively, in a period of $1s$, an E. coli cell will be displaced by $1\mu m$ and rotated in a $1/3$ rad angle, as a result of cumulative interaction with the medium. This is the reason why observed trajectories of bacteria are never on an entirely straight line [28]. The mean-square deviation in direction $\Delta\theta$ in a short interval Δt is

$$\left\langle \Delta\theta^2 \right\rangle = 2D_r\Delta t \tag{3.5}$$

where D_r is the rotational diffusion coefficient in rad^2/s and gives a measure of how a cell subject only to Brownian rotation would move, as if it is subject to a random force and torque. The mean rotational displacement is zero:

$$\langle \Delta\theta \rangle = 0 \tag{3.6}$$

Brownian rotation is implemented by sampling from a normal distribution with zero mean and standard deviation equal to $\sqrt{2D_r\Delta t}$ [26]. For chemotactic bacteria, Brownian rotation is only an added effect and slightly tweaks the facing direction of a motile swimming cell, reducing $\langle v_x(0)v_x(s)\rangle$, and therefore the effective correlation time and random motility coefficients D_x, D_y [8]. Even though we take Brownian rotation into account for our simulations, we ignore Brownian displacement, since its effect is weak compared to the displacement caused by swimming.

3.2 Kernel-type Reduced Models

As described in Chapter 2, there is a number of mathematical models for chemotaxis that express a series of internal processes and chemical signaling inside the cell into a single term Q. We focus on kernel models where Q is of the form

$$Q(t) = \int_{-\infty}^{t} K(t-s)C(s)ds \tag{3.7}$$

for some kernel function K and concentration function C. We investigate the validity of these models and compare their parameters and assumptions in benchmark cases of pulse, step change and linear gradient of attractant concentration. We also present the weak response estimates in [14,68] and come up with relationships between the parameters of these two reduced models we use in the simulations. We then explore the response model $F(Q)$ for the mean run time and depart from standard models for the mean run time or tumble rate in previous studies [14,29,37,68]. Lastly, we describe how we model a few additional features, namely: reorientation bias, finite tumble times and Brownian rotation. After setting up a 2D Markov chain Monte Carlo simulation, we test the PDE models' assumptions and discover different characteristics beyond the weak response level. We are motivated to explore stronger responses, because recent studies have observed higher chemotactic drift than expected in the weak response range [30,70].

The kernel models often aim to justify macroscopic PDE equations for a cell population starting from the individual response. In other words, they are asymptotically matched to a Keller-Segel-type equation, where the chemotactic drift and random motility are readily available as coefficients in (2.1) or an equation of similar form. One limitation of this formulation however, is that the Keller-Segel equations derived in this manner assume a weak response. In addition, this equivalence also justifies the claim that reduced models don't result in any change in the random motility, and μ in equation (2.1) is considered constant.

3.2.1 Calibration Between Models

Studying different models for the same phenomenon is challenging, especially when a lot of notation, assumptions and terminology are involved. We base our simulations mainly on the model described in [14] and verify that the model in [68] is equivalent. To that end, we calculate analytically the bias term $Q(t)$ presented by a cell according to each model, in three scenarios:

1. $C(s) = \delta_0(s)$, so that there is an instantaneous increase in the nutrients level at time $s = 0$. The models need to capture the excitation of the cell when subject to this condition.

2. $C(s) = H(s)$, where $H(s)$ is the Heaviside function, i.e. 0 for $s < 0$ and 1 for $s > 0$. This

test case corresponds to an increase of nutrients starting at time $s = 0$ and keeping the same level thereon. In this case, the models are tested for accurately describing adaptation to a new (higher) background concentration.

3. $C(s) = cs$, where $c > 0$, so that we model a cell swimming upstream a linear gradient. This case is meant to simulate the response of cells when swimming in an increasing nutrient concentration and is expected to present both excitation and adaptation.

The reasoning behind picking these test cases is that any model for the chemotactic response of E. Coli should have, at least to some degree, a form that agrees with the responses experimentally measured by Segall, Block and Berg to a pulse and step change in attractant concentration, shown in Figure 2.2 [49]. We start the calibration process across the two models by comparing the responses corresponding to the first two cases but the third case is needed to close the system and provide the proper scaling of the response. For both models and test cases, it is possible to make comparisons of points of extrema, limits and integrals of corresponding responses to match the values of involved parameters.

Here, we show the process we followed to compare the models in [14] and [68]. The kernel function for the first model is

$$K_{\mathrm{CV}}(t) = \beta_1 \lambda e^{-\lambda t} \left[\lambda t - \frac{1}{2} (\lambda t)^2 \right] \tag{3.8}$$

with parameters β_1 and λ. The baseline mean run time is denoted by τ_0, while the modified mean run time, due to chemotaxis, in $\tau = \dfrac{\tau_0}{1 - Q}$. The kernel function for the second model is

$$K_{\mathrm{XO}}(t) = \frac{b\tau_0}{t_e(t_a - t_e)} \left[t_a e^{-t/t_e} - t_e e^{-t/t_a} \right] \tag{3.9}$$

with parameters b, t_a, t_e. The same notation is used for the baseline mean run time τ_0 and the modified mean run time is extracted in the same manner, depending on the value of Q as $\tau = \dfrac{\tau_0}{1 - Q}$.

1. The response to a pulse is the kernel function itself, so

	$Q_C^\delta(t) = \beta_1 \lambda e^{-\lambda t}\left[\lambda t - \frac{1}{2}(\lambda t)^2\right]$	$Q_{\mathrm{XO}}^\delta(t) = \frac{b\tau_0}{t_e(t_a - t_e)}\left[t_a e^{-t/t_e} - t_e e^{-t/t_a}\right]$
point of maximum	$\frac{2-\sqrt{2}}{\lambda}$	0
root	$\frac{2}{\lambda}$	$\frac{t_e t_a \log\left(\frac{t_a}{t_e}\right)}{t_a - t_e}$
point of minimum	$\frac{2+\sqrt{2}}{\lambda}$	$\frac{2t_e t_a \ln(t_a/t_e)}{t_a - t_e}$
positive area	$\beta_1 e^{-2}$	$\frac{b\tau_0 t_a}{t_a - t_e}\left\{\left(\frac{t_a}{t_e}\right)^{-\frac{t_e}{t_a - t_e}} - \left(\frac{t_a}{t_e}\right)^{-\frac{t_a}{t_a - t_e}}\right\}$

From these results, and taking into account that $t_e \ll t_a$, we conclude that $\lambda \propto 1/t_a$, which is also consistent dimensionally, since λ has units of $\frac{1}{[t]}$ and t_a is a timescale.

We briefly mention that for a kernel of the form $K(t) = N\ell e^{-\ell t}\left(1 - \frac{1}{2}\ell t - \frac{1}{4}\ell^2 t^2\right)$ as in [17, 37], the point of maximum is 0, the root is $\frac{\sqrt{5}-1}{\ell}$, the point of minimum is $\frac{\sqrt{6}}{\ell}$ and the positive area is equal to $\frac{\sqrt{5}+1}{2} N e^{-\sqrt{5}+1}$.

2. The response to a step change is the anti-derivative of the response to a pulse, so all characteristic points have already been covered by case 1.

3. The response to a linear ramp, $C(s) = s$ gives us some measure of relationship between β_1 and b. We compute analytically

	$Q_C^s(t) = \frac{\beta_1 \lambda e^{-\lambda t}}{2\lambda}\left[2e^{\lambda t} - \lambda^2 t^2 - 2\lambda t - 2\right]$	$Q_{\mathrm{XO}}^s(t) = \frac{b\tau_0 t_a}{t_a - t_e}\left[(t_a - t_e) + t_e e^{-t/t_e} - t_a e^{-t/t_a}\right]$
$\lim_{t\to\infty}$	$\frac{\beta_1}{\lambda}$	$b\tau_0 t_a$

which in combination with $\lambda \propto 1/t_a$ leads to the conclusion that $\beta_1 \propto b\tau_0$.

In our simulations, we set the limit value for the maximum bias $Q_{\max}$ to be the limit value of $Q(t)$ under a linear gradient of attractant concentration, $C(s) = s$. As shown in the table above, $Q_{\max}$ is $\frac{\beta_1}{\lambda}$ for the first model and $b\tau_0 t_a$ for the second model.

Even though the above comparison points give us an insight on the role of each parameter in the model and in relation to each other, a more involved calculation is necessary to fully calibrate the two models. Therefore, we turn to the estimates for weak responses that are given by the authors of these two models [14,68]. They both use asymptotic analysis to reach a Keller-Segel type equation and express the chemotactic coefficient χ in terms of their parameters. More details about the asymptotic estimates and how they relate to this thesis are in Section 3.4.1.

For a weak response, if Brownian motion is ignored, the chemotactic coefficient divided by the square of the swim speed in the first model is

$$\frac{\chi_{\mathrm{CV}}}{v_s^2} = \frac{\beta_1}{d} \frac{\lambda^2 \tau_0^3}{\left[\lambda\tau_0 + (1 - \langle\cos\Phi\rangle)\right]^3} \tag{3.10}$$

and in the second model, assuming $t_e = 0$, it is

$$\frac{\chi_{\mathrm{XO}}}{v_s^2} = \frac{b}{d} \frac{t_a \tau_0^2}{\tau_0 + (1 - \langle\cos\Phi\rangle)\, t_a} \tag{3.11}$$

In both estimates d is the dimension (here $d = 2$), $\langle\cos\Phi\rangle$ is the mean cosine of the reorientation angle Φ and τ_0 is the baseline mean run time. We pick the parameter values appropriately, so that these two estimates match :

$$\beta_1 \frac{\lambda^2 \tau_0}{\left[\lambda\tau_0 + (1 - \langle\cos\Phi\rangle)\right]^3} = b \frac{t_a}{\tau_0 + (1 - \langle\cos\Phi\rangle)\, t_a} \tag{3.12}$$

$$\Rightarrow \quad b t_a \tau_0 = \beta_1 \frac{(\lambda\tau_0)^2}{\left[\lambda\tau_0 + (1 - \langle\cos\Phi\rangle)\right]^3} \left[\tau_0 + (1 - \langle\cos\Phi\rangle)\, t_a\right] \tag{3.13}$$

Using our calculations from the table on the third test case, we substitute the left hand side and get

$$\frac{\beta_1}{\lambda} = \beta_1 \frac{(\lambda\tau_0)^2}{\left[\lambda\tau_0 + (1 - \langle\cos\Phi\rangle)\right]^3} \left[\tau_0 + (1 - \langle\cos\Phi\rangle)\, t_a\right] \tag{3.14}$$

and solving for t_a, we get

$$t_a = \frac{\left[\lambda\tau_0 + (1 - \langle\cos\Phi\rangle)\right]^3 - \lambda^3\tau_0}{\lambda^3 \tau_0^2 \left(1 - \langle\cos\Phi\rangle\right)} \tag{3.15}$$

When using the model in [14], we use the value for $\lambda = 2s^{-1}$ and β_1 is determined by the value of $Q_{\max}$. To use the model in [68], we compute t_a by (3.15) and b by

$$b = \frac{\beta_1}{\lambda t_a \tau_0} \tag{3.16}$$

The resulting simulations produce very close results in the same conditions, even when Brownian motion is added.

The bias function $Q(t)$ is the convolution of the kernel with the concentration history. In order to make sure that Q is dimensionless, K has to be defined in units of $\frac{1}{[C][t]}$, where $[C]$ denotes concentration units and $[t]$ units of times. A little dimension analysis of the terms involved in (3.8) and (3.9) yields that β_1 is defined in units of $\frac{1}{[C]}$ and b is defined in units of $\frac{1}{[C][t]}$. The result (3.10) gives a working range of plausible values for λ :

- if $\lambda\tau_0 \gg 1$, then the resulting drift is in the order of $\frac{1}{\lambda\tau_0}$. This corresponds to very fast adaptation timescale, so that a potential chemotactic effect will not last long enough to cause an effective drift.

- if $\lambda\tau_0 \ll 1$, then the resulting drift is in the order of $\lambda^2\tau_0^2$. This corresponds to slow adaptation, where even small increases or decreases in the attractant concentration will affect the run time over a large timescale.

Both cases result in too small drift, indicating that λ and τ_0 must be comparable for an optimal response, as illustrated in Figure 3.2.

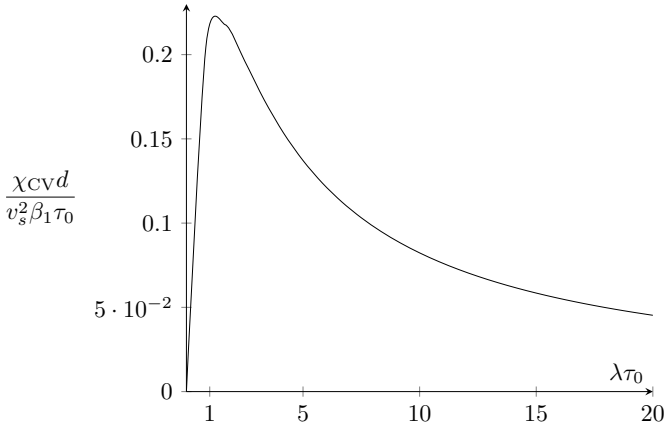

Figure 3.2: The chemotactic coefficient divided by some of the parameters of the first model from [14] and multiplied by the dimensions d versus the product of parameter λ with τ_0. Chemotactic drift is stronger when $\lambda\tau_0$ are of the same magnitude and the corresponding maximum is global. For small or large values of $\lambda\tau_0$, the chemotactic coefficient drops, relative to its maximum value. Both axes are non-dimensional.

3.2.2 Response Functions

In the absence of nutrients in their environment, E. Coli cells run-and-tumble with a baseline mean run time τ_0. However, the mean run time is modified according to external stimuli : if moving towards better conditions, it will increase, while if moving towards worse conditions, it will decrease. As prefaced in Chapter 2, the reduced models use the bias term Q to achieve these modifications in the duration of runs, according to extracellular stimuli. In particular, the mean run time at time t is given in the form

$$\tau(t) = \tau_0 F(Q(t))$$

for some appropriate choice for the response function F. The usual assumptions are that F is larger than 1 for positive values of Q and the mean run time increases from the baseline τ_0, whereas F is smaller than 1 for negative values of Q and the mean run time is shortened. The

response function F must also be increasing, allowing for stronger or weaker responses based on the value of Q.

It has also been observed that wild-type E. Coli increase their run times more significantly than they decrease them, so F must present some type of asymmetry with respect to the $y = 1$ line [13].

For our simulations, we use the response functions that are common in the literature but also investigate a few others

$$F_1(Q) = 1 + Q \tag{3.17}$$

$$F_2(Q) = (1 - Q)^{-1} \tag{3.18}$$

$$F_3(Q) = e^Q \tag{3.19}$$

$$F_4(Q) = \frac{1 + e^{2Q}}{2} \tag{3.20}$$

$$F_5(Q) = \begin{cases} 1 + Q, & Q \geq 0 \\ 0, & Q < 0 \end{cases} \tag{3.21}$$

On one hand, we check if a symmetric linear model would result in an efficient chemotactic response (3.17). On the other hand, we propose asymmetric response functions (3.19) and (3.20), and one extreme response function where runs are only allowed to be lengthened but not shortened (3.21). The response model $F_2(Q)$ is standard in existing models [14, 37, 68], and the same holds for $F_3(Q)$ [3, 29].

All of them capture the behavior of increasing τ for positive Q and decreasing τ for negative Q (with respect to the baseline mean run time τ_0). In addition, their values are close for small amplitude responses ($|Q| < 0.3$). Further out, they differ in the amount of asymmetry between increased and decreased runs (see Figure 3.3).

We compare the performance of all these response functions in terms of chemotactic drift and population diffusion. For a meaningful study, we need to move from the weak response area of $|Q| < 0.3$ and allow for more substantial changes in the mean run time, as recent experimental work has shown that stronger responses are attainable [70]. One more reason that motivates us to extend our study to higher values of Q is to verify if the asymptotic approximations by [14,37,68] still hold outside the weak response regime.

3.2.3 Reorientation Bias

Research findings show that when cells reorient ("tumble"), the new direction follows some axisymmetric distribution Φ, so that there is some directional bias during tumble events. We

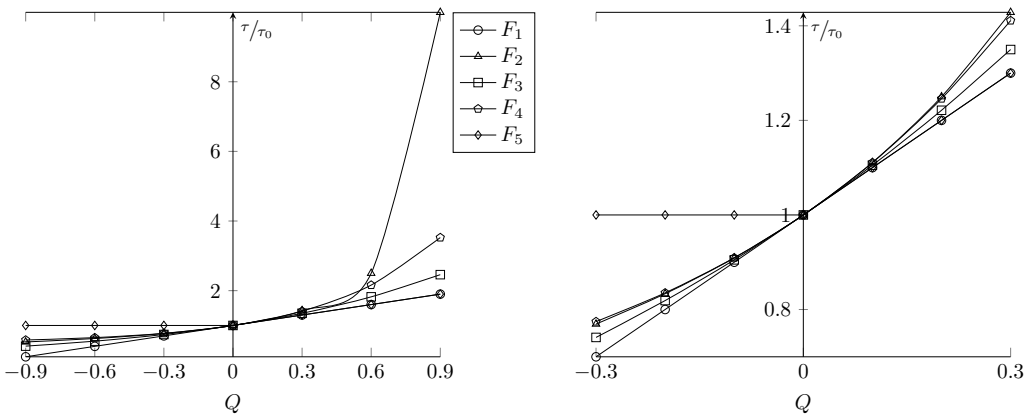

Figure 3.3: Graphical comparison of options for response function F for values of Q in $[-0.9, 0.9]$ (left) and in $[-0.3, 0.3]$ (right).

test the effect of the specific distribution to chemotactic efficiency and to velocity autocorrelation. We have considered several distributions for Φ :

1. $\Phi \sim \mathcal{U}[-\alpha, \alpha]$ corresponds to a limited range of uniformly weighted angles in a symmetric interval. This choice introduces some reorientation bias in the sense that only part of the available directions are considered.

2. $\Phi \sim \widehat{\mathcal{N}}\left(0, \sigma^2\right)$, where $\widehat{\mathcal{N}}$ is the normal distribution defined on $[-\pi, \pi]$ and rescaled appropriately.

3. $\Phi \sim \mathcal{U}[-\pi, \pi]$ corresponds to isotropic reorientations. We examine how the overall drift towards more attractants is affected if the cell doesn't show preference to a particular direction.

4. $\Phi \sim$ Von Mises$(0, k)$ or circular normal distribution. There is a probability to sample any direction but the ones closer to 0 are more likely. The Von Mises distribution is very close to wrapped normal distribution and its definition involves the modified Bessel function of the first kind.

5. $\Phi \sim f_\Phi$ where f_Φ is the distribution in Figure S8 of [14], similar to the one obtained in [49]. We extract the data points from the figure with the Matlab package `grabit` and then fit that distribution to a sum of two exponential terms $ae^{b\phi} + ce^{d\phi}$.

The mean, variance and higher moments of the last three distributions of Φ can be analytically derived. That calculation can be used to match the parameters of the reorientation distribution used to experimental observations. For E. Coli, it is known that $\langle \cos \Phi \rangle \simeq 0.33$. This information is used to determine the values of α and k for the uniform and Von Mises distributions above and scale f_Φ appropriately. In particular, simple calculations show that the mean cosine of Φ

for the reorientation distributions mentioned above is

$$\frac{1}{2\pi}\int_{-\pi}^{\pi}\cos\phi\,\mathrm{d}\phi = 0 \tag{3.22}$$

$$\frac{1}{2\alpha}\int_{-\alpha}^{\alpha}\cos\phi\,\mathrm{d}\phi = \frac{\sin\alpha}{\alpha} \tag{3.23}$$

$$\frac{1}{2\pi I_0(k)}\int_{-\pi}^{\pi}\cos\phi\cdot e^{k\cos\phi}\,\mathrm{d}\phi = \frac{I_1(k)}{I_0(k)} \tag{3.24}$$

$$\int_{-\pi}^{\pi}ae^{b\phi}+ce^{d\phi}\,\mathrm{d}\phi = -\frac{2ab\sinh(b\pi)}{b^2+1}-\frac{2cd\sinh(d\pi)}{d^2+1} \tag{3.25}$$

Since the mean cosine is known, we need to set the corresponding quantity (right-hand sides of equations (3.23), (3.24) and (3.25)) to that value and solve for the parameter(s) of the distribution. In our simulation, this was achieved by solving a non-linear equation with the built-in function of Matlab `fzero`.

As mentioned earlier in Section 3.1, reorientation bias leads to longer autocorrelation times and these translate to longer memory scale, in other words: how long the effect of a detected change in stimuli lasts on the future behavior of a cell. The velocity autocorrelation decays exponentially with time. We estimate the rate of this decay for all reorientation models for the distribution of Φ, the random variable representing the change in direction between runs in our simulations, including the isotropic unbiased option for reference. The results are in Table 3.1.

distribution of Φ	a	ρ
$\mathcal{U}[-\pi,\pi]$	0.4879	1.019
$\mathcal{U}[-\alpha,\alpha]$	0.4970	0.747
Von Mises$(0,k)$	0.5002	0.690
f_Φ	0.5066	0.689

Table 3.1: The parameters of an exponential curve fitting to the values of $\langle\cos\theta(0)\cos\theta(t)\rangle$ of the form $ae^{-\rho t}$. The fitting was done by the `fit` built-in Matlab function with the `exp1` option and default tolerance parameters on data from a random walk with $N = 5000$, $T = 50s$, $\Delta t = 0.01s$. All distributions except for $\mathcal{U}[-\pi,\pi]$ were defined so that $\langle\cos\Phi\rangle = 0.33$.

3.2.4 Simulation Methods

To test our model, we set up a simulation of N swimmers performing a 2D random walk starting at the origin. At every time step, we update their location according to the most recently picked direction and check if they will tumble; if they do, we change their direction according to $\theta_{\text{new}} = \theta_{\text{old}} + \Phi$. We model the random event of tumbling as a Poisson process, so that for a

Algorithm 1 Pseudocode for the 2D random walk : kernel model

```
for i = 1, ··· , N do
    (X_{i,1}, Y_{i,1}) ← (0, 0)
    θ_{i,1} ← U[−π, π]
    for j = 1, ··· , M − 1 do
        (X_{i,j+1}, Y_{i,j+1}) ← (X_{i,j}, Y_{i,j}) + Δt v_s (cos θ_{i,j}, sin θ_{i,j})
        update Q
        update τ = τ_0 F(Q)
        if rand()< dt/τ then
            θ_{i,j+1} = θ_{i,j} + Φ
        else
            θ_{i,j+1} = θ_{i,j}
        end if
        θ_{i,j+1} = θ_{i,j+1} + randn()√(2D_r Δt)
    end for
end for
```

mean run time duration τ, the probability of tumbling in an interval of length Δt is $\frac{\Delta t}{\tau}$. The mean run time τ can differ from the baseline mean run time τ_0, according to $\tau = \tau_0 F(Q)$ for the response models discussed in Section 3.2.2 that extend runs in a good direction and shorten runs in a bad direction (except for F_5).

Some extra elements that we added to the random walk presented in the pseudocode in Algorithm 1 are finite tumble times and Brownian rotation. To include finite tumble times, we freeze a cell in place while tumbling for a number of time steps, so that the overall time for a tumble follows an Exp(0.1) distribution, that is independent of the level of chemoattractants or the previous trajectory of the cell. The only addition to the pseudocode is to sample a tumble duration $W \sim \text{Exp}\,(0.1)$ and freeze the cell in place for the next $\left\lceil \frac{W}{\Delta t} \right\rceil$ timesteps. For a sufficiently low Δt, we get an accurate approximation of the correct duration of tumble times.

To simplify the analysis and imitate the configurations in the majority of experiments, we assume that there is a change of the level of attractants only in the x direction and no change in the y direction, i.e. $\nabla C\,(x, y) = (c_1, 0)$. This enables us to focus on the characteristics on only one component of the position data over the random walk. More details on this analysis follow in Section 3.3.

3.3 Data Analysis

To validate our models and cross-check results with similar experimental outcomes, we use the *drift velocity* and *motility coefficient* as population-scale transport parameters. These are common quantities that measure the effect of chemotaxis on a cell population : the drift velocity v_{drift} corresponds to the speed of the center of mass of a cell population, in other words, how fast a population moves up a concentration gradient on average. The motility coefficient D_x measures

how spread out in the x direction the population is. We are interested in these two quantities, because they are widely used in experimental studies as well. In our simulation, we compute the y component of the velocity of the center of mass, which is expected to be zero in our setup : there is no attractant concentration change, so there is no reason to see a preference moving to positive or negative y direction. We also investigate the effect of chemotaxis on the diffusion of a cell population. The swimming cells are expected to spread out over time and, intuitively, they should be more dispersed in the direction of increasing attractants. The asymptotic estimates in [14,68] don't predict any change in diffusion from the non-chemotactic case, which contradicts this argument. Therefore, we compare D_x to D_y, the motility coefficient in the y direction, to check if a gradient purely in one dimension affects the isotropic spread that is observed in a homogeneous environment.

3.3.1 Parameter Estimation of Drift Velocity and Motility Coefficient

The diffusion coefficients in x and y direction, D_x and D_y respectively, and the drift velocity in the positive x direction v_{drift} are estimated using the fact that they have a connection with position variances and means.

For a $2D$ diffusion process, it can be shown that $\text{Var}\left(X(t)\right) = 2D_x t$ in the longterm [20]. For a random walk simulation, D_x can be estimated by

$$D_x = \lim_{t\to\infty} \frac{\text{Var}\left(X(t)\right)}{2t}$$

We have used the fact that after some transition interval in the beginning of the random walk, $\text{Var}\left(X_j\right)$ becomes linear with time [31], where X_j is the vector of cell X locations at time $j\Delta t$ (j-th timestep), so an estimator θ_{D_x} of D_x is given by

$$\theta_{D_x} = \frac{\text{Var}\left(X_b\right) - \text{Var}\left(X_a\right)}{2\Delta t(b-a)}$$

for b and a large enough, so that they are in the linear regime. Using the unbiased estimators for the variances

$$S_{X,b} = \frac{1}{N-1}\sum_{i=1}^{N}\left(X_{i,b} - \bar{X}_b\right)^2$$

and

$$S_{X,a} = \frac{1}{N-1}\sum_{i=1}^{N}\left(X_{i,a} - \bar{X}_a\right)^2$$

where N is the number of cells, $X_{i,j}$ is the X position of the i-th cell at the j-th timestep and $\bar{X}$

denotes the sample mean, i.e. the mean across i, we can also find confidence intervals for θ_{D_x} as

$$\theta_{D_x} = \frac{S_{X,b} - S_{X,a}}{2\Delta t(b-a)} \pm z^\star \frac{1}{\Delta t\,(b-a)} \sqrt{\frac{S_{X,b}^2 + S_{X,a}^2}{2\,(N-1)}} \tag{3.26}$$

for $z^\star$ the z-score corresponding to a desired confidence level. Eg. for 95%, $z^\star = 1.96$; for 99%, $z^\star = 2.58$. Z-test is applicable, because X_j follows an approximately normal distribution for all j. To minimize the variance of the estimator, b and a should be chosen as far apart as possible. Therefore, we computed our estimates using $b =$ the number of timesteps and $a = 0.3b$. Similarly for D_y

$$\theta_{D_y} = \frac{S_{Y,b} - S_{Y,a}}{2\Delta t(b-a)} \pm z^\star \frac{1}{\Delta t\,(b-a)} \sqrt{\frac{S_{Y,b}^2 + S_{Y,a}^2}{2\,(N-1)}} \tag{3.27}$$

A similar process can be used to estimate v_{drift}, since

$$v_{\text{drift}} = \lim_{t \to \text{inf}} \frac{\langle X(t) \rangle}{t}$$

Our simulations show that after some transition interval in the beginning of the random walk, $\langle X_j \rangle$ becomes linear with time, so we use the estimator θ_v of v_{drift}

$$\theta_v = \frac{\langle X_b \rangle - \langle X_a \rangle}{\Delta t\,(b-a)}$$

and plugged in the unbiased estimators for the means

$$\bar{X}_b = \frac{1}{N} \sum_{i=1} X_{i,b}$$

$$\bar{X}_a = \frac{1}{N} \sum_{i=1} X_{i,a}$$

which leads to the following estimate with confidence intervals

$$\theta_v = \frac{\bar{X}_b - \bar{X}_a}{\Delta t(b-a)} \pm z^\star \frac{1}{\Delta t\,(b-a)} \sqrt{\frac{S_{X,b} + S_{X,a}}{N}} \tag{3.28}$$

3.4 Results

In Figures 3.5, 3.6, 3.7, 3.8 and 3.9, we present the simulation results for $\frac{v_{\text{drift}}}{v_s}$(left) and D_x(right) for the response functions F_1, F_2, F_3, F_4, F_5 noted in Section 3.2.2 and compared to the asymptotic estimates in [14].

First of all, it is clear that the dynamics of the random walk depend on the choice of response function $F(Q)$. The linear model F_1, where the amount of decrease in run times

symbol	meaning	value
N	number of swimmers	10000
T	duration of simulation [s]	50
Δt	timestep of random walk [s]	0.01
τ_0	baseline mean runtime [s]	1
v_s	swimming speed [μm]/[s]	25
τ_t	mean tumble time [s]	0
λ	scaling parameter of model in [14] $[s]^{-1}$	2
$\langle \cos \Phi \rangle$	mean cosine of reorientation angle Φ	0.33
c_1	linear coefficient of concentration function [μM/μm]	0.4
D_r	Brownian rotation coefficient $[rad]^2/[s]$	0.062
CL	confidence level	95%

Table 3.2: Input parameters for simulations.

is symmetric to the amount of their increase, results in drift velocity close to the estimate and the motility coefficient falls close or is somewhat smaller, depending on the reorientations distribution. However, in reality, an asymmetry is expected: runs directed up a gradient of attractants are significantly longer than the baseline runtime, while runs in an unfavorable direction, down a gradient of attractants, are not shortened to the same extent [11, 46, 47]. The asymmetrical response models $F_2(Q)$ and $F_4(Q)$ depicted in Figures 3.6 and 3.8 capture this asymmetry.

We also test the chemotactic efficiency of the extreme strategy of not shortening unfavorable runs at all, which results in almost half of the chemotactic velocity of the other models and slightly increased motility (Figure 3.9). We therefore conclude that shortening "bad" runs is essential for efficient chemotaxis, as indicated by our random walk simulations.

3.4.1 Comparison to Weak Response Approximations

In Section 3.2.1, we briefly mentioned that comparing the asymptotic estimates of the two reduced models [14,68], we complete the calibration process. Both models start from an individual-cell description (see (2.7), (2.10)) and derive a Keller-Segel system of PDEs for the density of cells and nutrients, resulting in an estimate for the chemotactic coefficient χ and motility coefficient μ in (2.1). The chemotactic velocity is then $\chi \nabla C(x, y)$, which in our case is $\chi\,(c_1, 0)$. The diffusion coefficient of a population of bacteria when moving in d dimensions in a homogeneous medium, considering instantaneous tumbles is given in [8, 38] :

$$D_x = D_y = \frac{v_s^2 \tau_0}{d\,(1 - \langle \cos \Phi \rangle)} \tag{3.29}$$

The models we examine claim that the motility coefficient will not change even when performing chemotaxis. Furthermore, as already mentioned in Section 3.2.1, the reduced models correspond to a Keller-Segel model assuming the response is weak, with a specific drift velocity that we can compute in each case via (3.10) and (3.11) and compare to the simulation outcomes.

One of the goals of this thesis, is to check if the asymptotic estimates obtained in this manner are a good approximation to effective drift and motility of stronger responses, where $Q > 0.3$. We ran simulations of bacteria swimming in 2D using both models. Because of the calibration process we presented earlier in Section 3.2.1, the two models produce close results, so only the ones based on [14] are presented in the following figures. Other input parameters of our simulations are in Table 3.2. We compare the normalized drift velocity $\frac{v_{\text{drift}}}{v_s}$ and the diffusion coefficient in the x direction obtained by the methods in Section 3.3.1 to equations 2.8 and 3.29 respectively.

In Figures 3.5, 3.6, 3.7, 3.8 and 3.9, the asymptotic estimates are plotted in magenta, two per graph: one to be compared to unbiased reorientations (low drift and motility) and one to be compared to biased reorientations (higher drift and motility). The value of the asymptotic estimate for the random motility coefficient in the former case is $\frac{v_s^2\tau_0}{2} = 312.5\mu m^2/s$, while in the latter case it is $\frac{v_s^2\tau_0}{2(1-0.33)} \approx 466\mu m^2/s$. These estimates are calculated and compared to simulations without Brownian rotation (plots are omitted). When Brownian rotation is included, random motility is reduced from these values to $\sim 294.26\mu m^2/s$ and $426.91\mu m^2/s$ respectively. The rest of the lines correspond to a different distribution for Φ, according to the legend in Figure 3.4. Each pair of graphs corresponds to a different response model: $F_1(Q), F_2(Q), F_3(Q), F_4(Q)$ and $F_5(Q)$ respectively.

We conclude that the asymptotic estimates hold in the weak response regime $Q_{\max} \leq 0.3$ but above that level, significant differences appear between the drift and motility derived by the kernel models and the simulated experiments, suggesting they are not sufficient to model stronger responses, as the ones observed in recent studies [30, 46, 70].

In the special case of $F_5(Q)$ (Figure 3.9), the magenta lines correspond to the same asymptotic estimate as the rest of the response models. The resulting drift is almost halved and motility is increased, indicating that if a hypothetical strain of bacteria used this strategy, they wouldn't be as efficient in detecting a source of attractants as the ones reducing run times in the wrong direction.

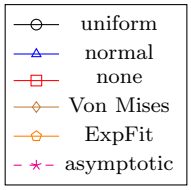

Figure 3.4: Legend for Figures 3.5, 3.6, 3.7, 3.8, 3.9.

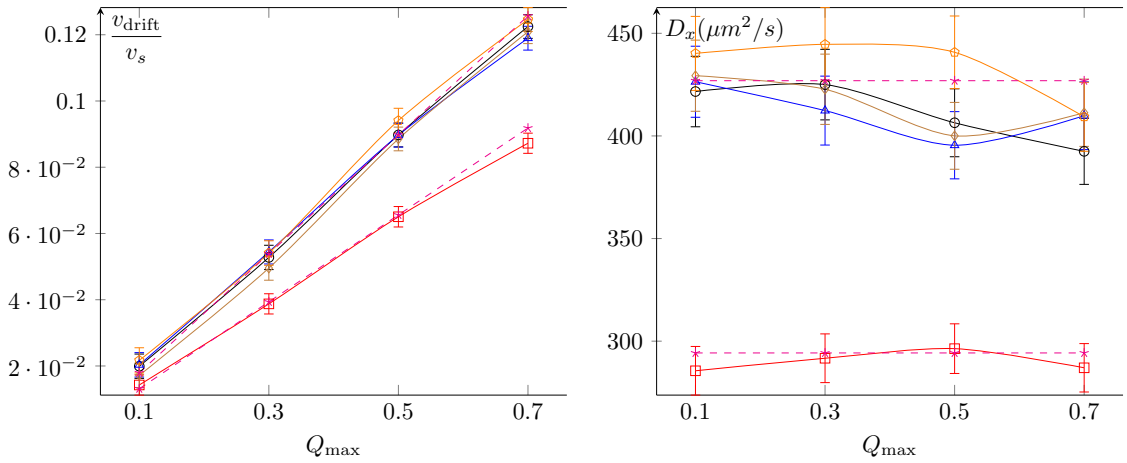

Figure 3.5: Comparison of simulation results for different distributions of Φ to asymptotic estimates in [14, 68]. $\frac{v_{\text{drift}}}{v_s}$(left) and D_x (right) when $F(Q) = F_1(Q) = 1 + Q$.

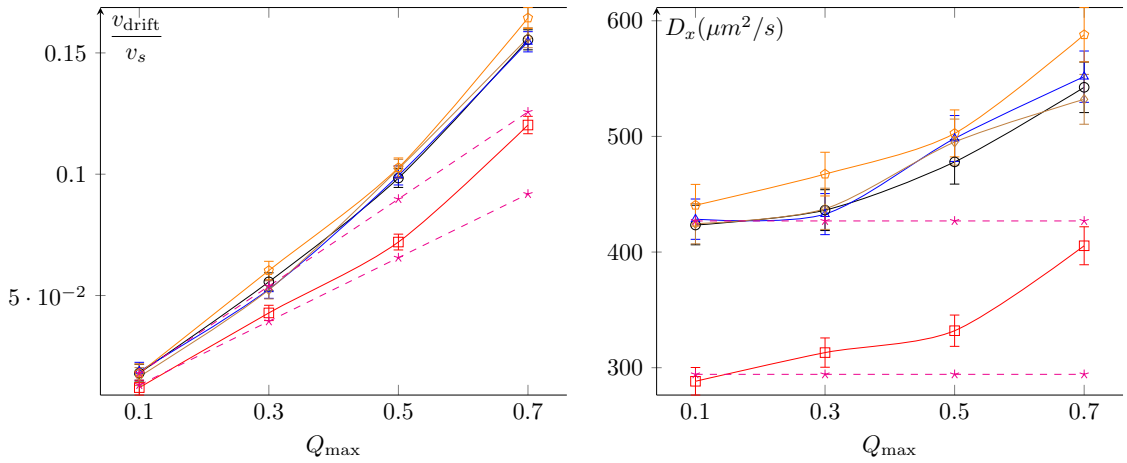

Figure 3.6: Comparison of simulation results for different distributions of Φ to asymptotic estimates in [14, 68]. $\frac{v_{\text{drift}}}{v_s}$(left) and D_x (right) when $F(Q) = F_2(Q) = \dfrac{1}{1-Q}$.

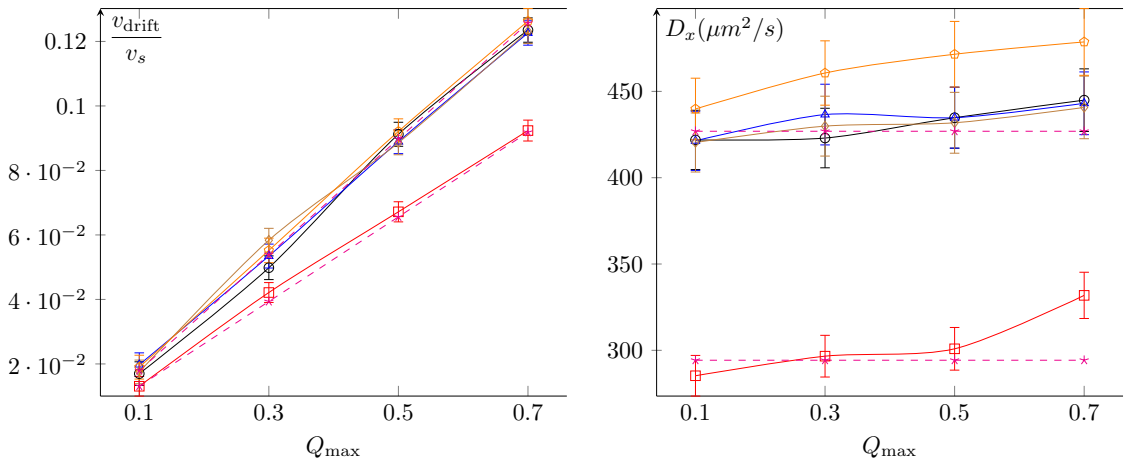

Figure 3.7: Comparison of simulation results for different distributions of Φ to asymptotic estimates in [14, 68]. $\frac{v_{\text{drift}}}{v_s}$(left) and D_x (right) when $F(Q) = F_3(Q) = e^Q$.

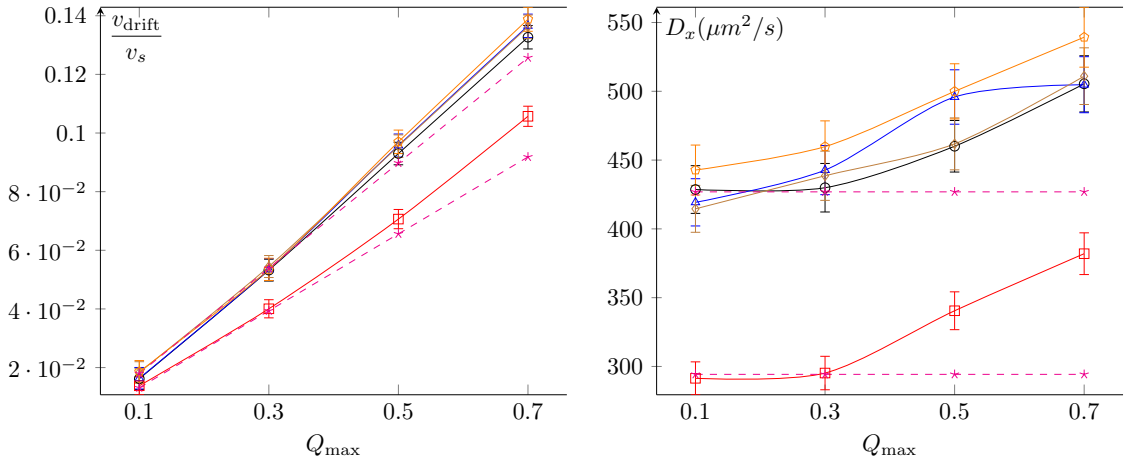

Figure 3.8: Comparison of simulation results for different distributions of Φ to asymptotic estimates in [14, 68]. $\frac{v_{\text{drift}}}{v_s}$(left) and D_x (right) when $F(Q) = F_4(Q) = \dfrac{1+e^Q}{2}$.

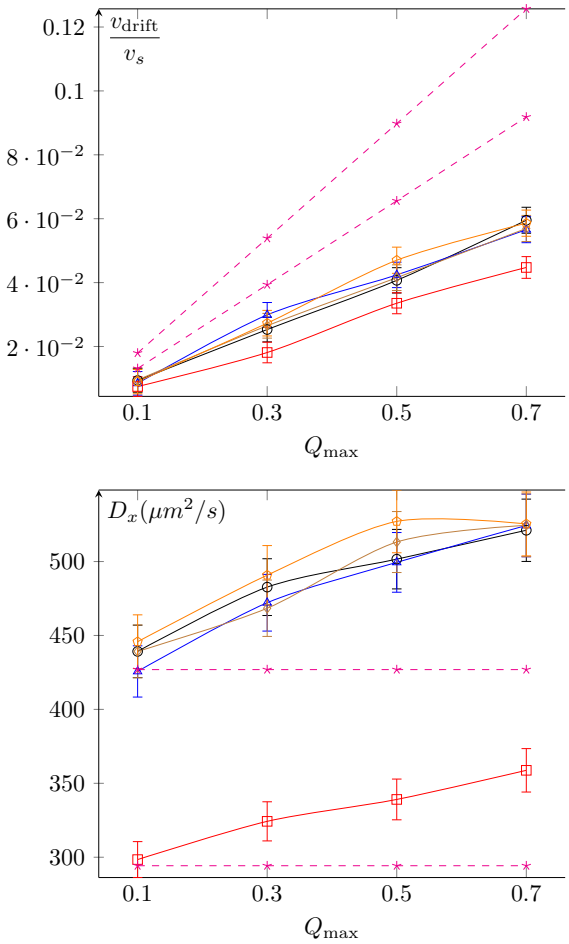

Figure 3.9: Comparison of simulation results for different distributions of Φ to asymptotic estimates in [14, 68]. $\frac{v_{\text{drift}}}{v_s}$ (top) and D_x (bottom) when $F(Q) = F_5(Q) = 1 + Q$ if $Q > 0$; 1 otherwise.

3.4.2 Diffusion Asymmetry

The asymptotic analyses for weak response in [14, 68], conclude that the existence of a linear gradient doesn't affect the diffusion of a bacterial population and that it basically remains unchanged from its baseline value in both dimensions:

$$D_x = D_y = \frac{v_s^2 \tau_0}{d\,(1 - \langle \cos \Phi \rangle)}$$

Our simulation results indicate that this is true for weak responses ($Q_{\max} \leq 0.3$) but stronger responses result in significant differences between the spreads of a population in x and y direction. Using a different mark notation (see caption in Figure 3.10), we present the estimates for D_x versus D_y corresponding to a Von Mises and f_Φ distribution of Φ, together with an auxiliary identity line (dashed magenta), for increasing value of $Q_{\max}$, from weaker to stronger response.

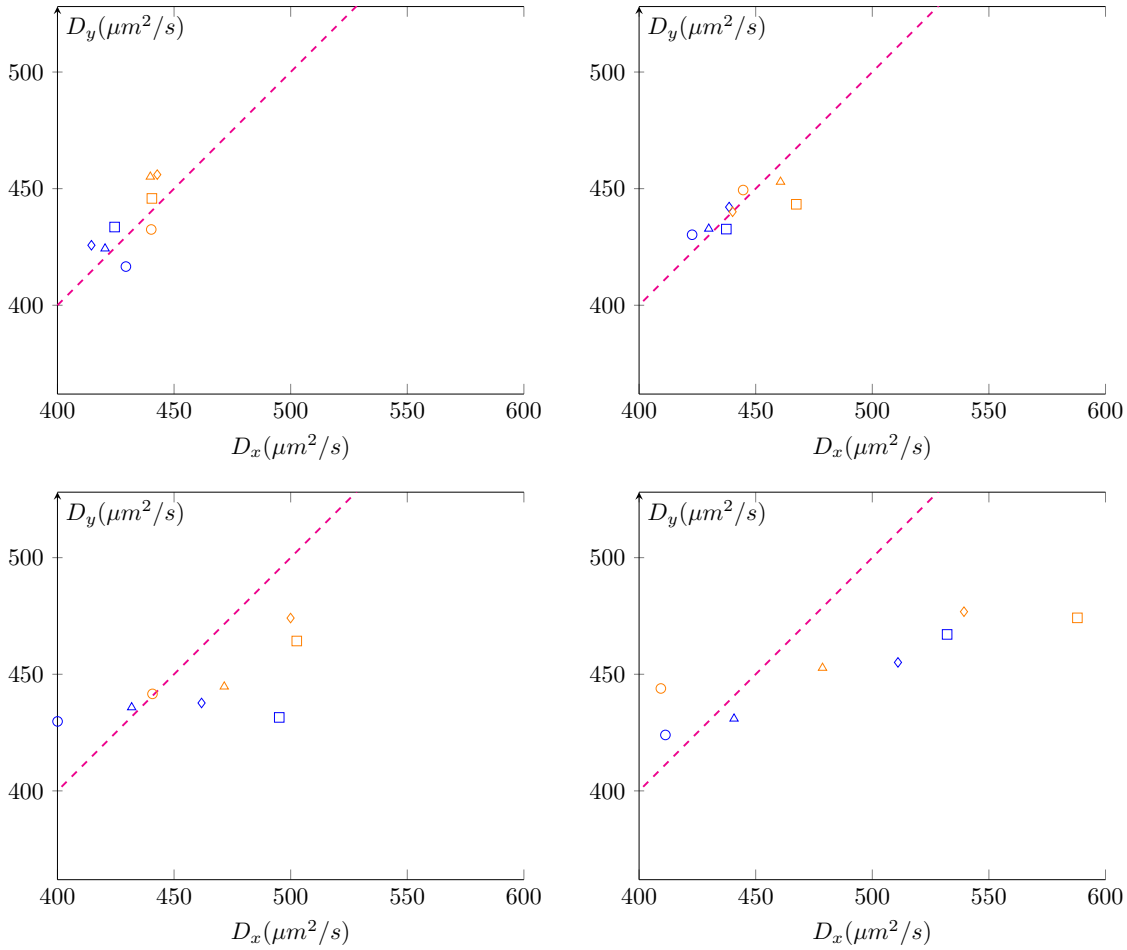

Figure 3.10: D_x versus D_y estimates from simulations with input parameters as in Table 3.2. All choices of mean run time model $F(Q)$, except for F_5, and Von Mises (in blue) and f_Φ (in orange) reorientations are plotted for $Q_{\max} = 0.1$ (top left); $Q_{\max} = 0.3$ (top right); $Q_{\max} = 0.5$ (bottom left); $Q_{\max} = 0.7$ (bottom right). The shape of markers denotes the response model: circle for F_1; square for F_2; triangle for F_3; diamond for F_4. Confidence intervals in both directions are of the order of 18 and omitted for the sake of clarity.

We also want to examine the effect of the runtime model used. In all cases presented in Figure 3.10, the estimates that fall closer to the identity relation are with the runtime models $F_1(Q) = 1 + Q$ (circle) and $F_3(Q) = e^Q$ (triangle), while more asymmetry is observed for the more asymmetrical models F_2, F_3. This indicates that the asymptotic limit for equal motility in the two principal directions at weak responses does not hold for stronger responses. In other words, we observe anisotropic dispersion when a gradient in one direction is added and the population is expected to form an ellipsoid shape instead of a circular one.

3.4.3 Effect of Finite Tumble Time

So far, all the results and analysis we mentioned assumed that the tumbles in our random walk simulations were instantaneous, a modeling assumption that is very common [14, 68]. However, in reality, tumbles have a finite duration that is short compared to the typical runtime. Since

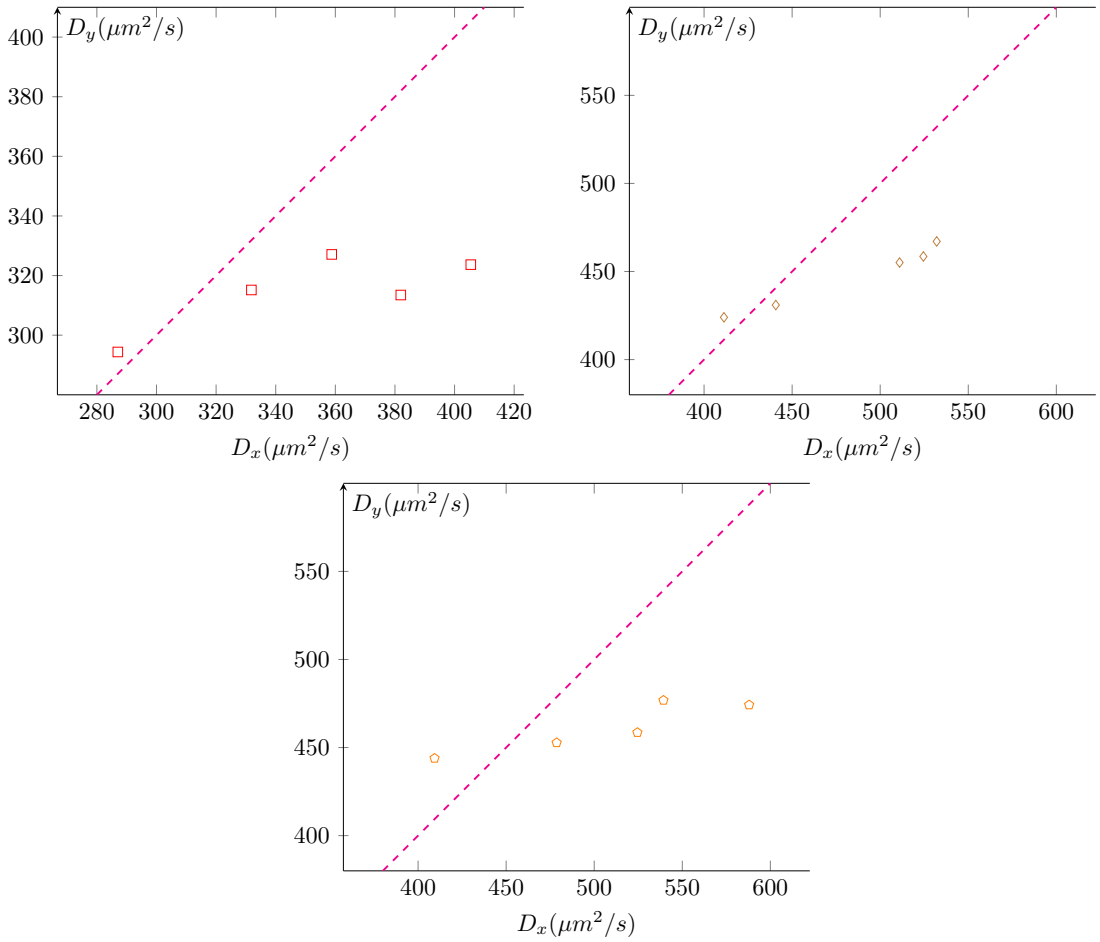

Figure 3.11: D_y versus D_x with a strong response $Q_{\max} = 0.7$ and no reorientation bias (top left); Von Mises reorientation distribution (top right); $\Phi \sim f_\Phi$ (bottom). Note the lower diffusion in the top left panel.

during a tumble the cell doesn't move at all, we are inclined to believe that the effect of a finite tumble time will just slow the overall random walk down and, as a result, scale down the drift velocity and motility by some factor. To test that claim, we also ran random walk simulations with finite tumble time that was exponentially distributed with mean $\tau_t = 0.1s$, a distribution that was documented in [10] and remains unchanged with attractant levels. According to [14], the motility coefficient is scaled by a factor of $\frac{\tau_0}{\tau_0 + \tau_t}$; they also calculate the modified chemotactic velocity. We only present simulation results for selected cases in Figure 3.12.

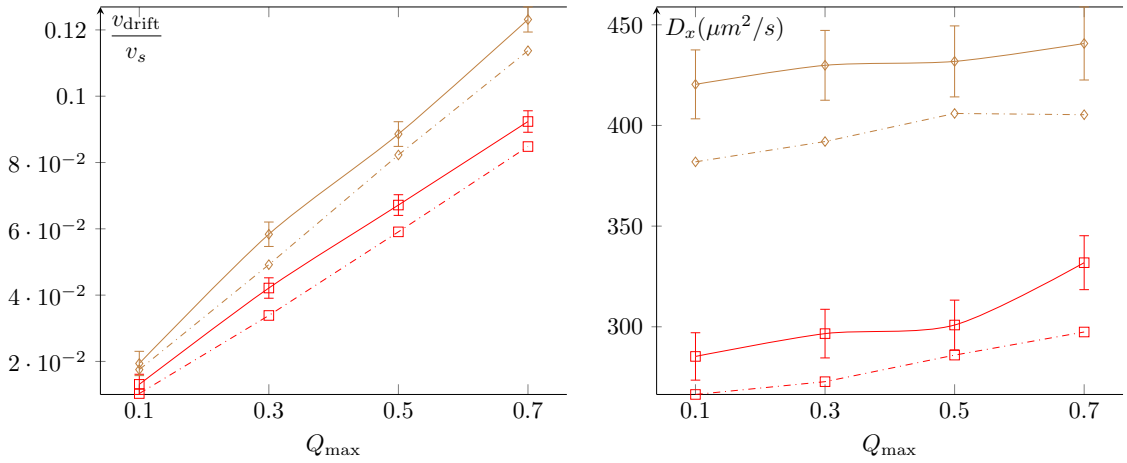

Figure 3.12: Normalized drift velocity (left) and motility coefficient D_x for the runtime model $\tau = \tau_0 e^Q$ and instantaneous tumbles (solid lines) or Exp (0.1) tumble times (dash-dotted lines). The brown lines correspond to Von Mises reorientations and the red lines to unbiased reorientations. Confidence intervals for the dash-dotted lines are omitted but they are of the same order as the ones on solid lines.

Finite tumble time results in a decrease in the drift velocity and diffusion coefficient compared to the instantaneous tumbles case. Despite small fluctuations, the scaling factor of $\frac{\tau_0}{\tau_0 + \tau_t} \sim 0.91$ is consistent in all of our simulation results, even the ones not presented in Figure 3.12.

3.4.4 Comparison to p^+, p^- Approximations

In their 1998 paper [16], the authors came up with estimates for the drift velocity and motility by perturbing Alt's cell-balance equations [5]. Alt's initial model was three-dimensional, and Ford and Cummings studied their relationship to a one-dimensional counterpart [25]. A similar approach was employed by Schnitzer [48] but he was still studying the equations on higher dimensions.

The alternative way to extract a population-scale motility coefficient and drift velocity is formulated in terms of the mean tumble rate, conditional on motion up the gradient (p^+) or conditional on motion down the gradient (p^-). The estimates are based on mapping the problem to a corresponding one-dimensional system with a gradient of concentration and motion along

a line and end up as

$$D_x = \frac{32}{3\pi^2}\frac{v_s^2}{(p^- + p^+)(1 - \langle\cos\Phi\rangle)} \tag{3.30}$$

$$\frac{v_{\text{drift}}}{v_s} = \frac{8}{3\pi}\frac{p^- - p^+}{p^- + p^+} \tag{3.31}$$

The related approximate analysis is best justified for a weak chemotactic response. These estimates have been used in later experimental studies eg. [3, 70], to measure drift velocity and random motility of three-dimensional trajectories tracked in free flows of bacteria in channels of linear gradient of chemoattractants.

Here, we compare our estimates (3.26) and (3.28) to (3.30) and (3.31) in Figures 3.13 and 3.14 for two options of Φ distributions and the asymmetrical response model $F_4(Q)$. The benefit of using (3.26) and (3.28) instead of (3.30) and (3.31) is that we only need to keep track of the locations of all cells in the simulation for two timesteps, instead of the extra calculation of p^+, p^- which requires saving all mean run times per direction throughout the simulation. Another drawback of this method is that it doesn't provide any information about the diffusion in the y-axis and how it compares to μ, since it only considers the 1D distinction of "left or right".

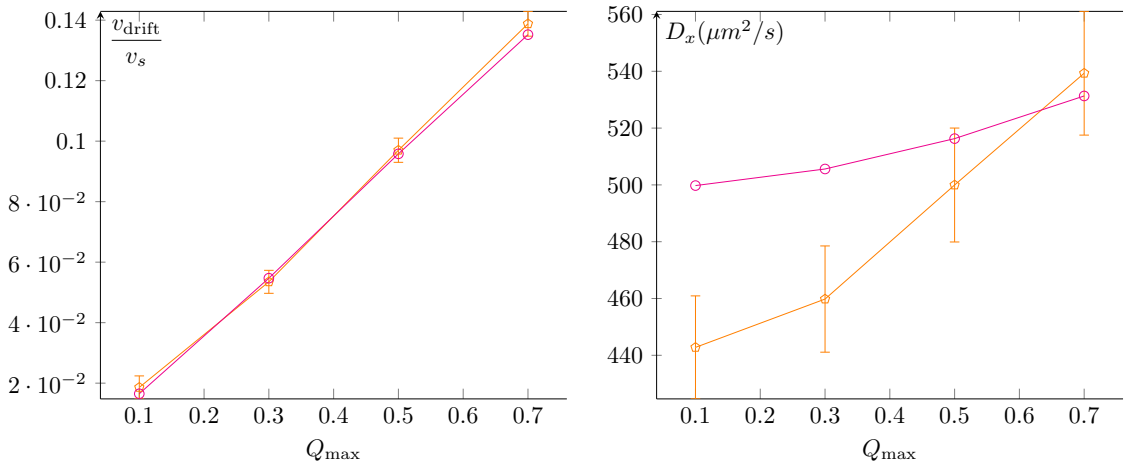

Figure 3.13: Comparison between estimates (3.28) and (3.31) (left) and (3.26) and (3.31) (right) with reorientations $\Phi \sim f_\Phi$ and $F(Q) = F_4(Q) = \frac{1 + e^{2Q}}{2}$. The orange line is our simulations results and the magenta line is the estimate using p^+ and p^-.

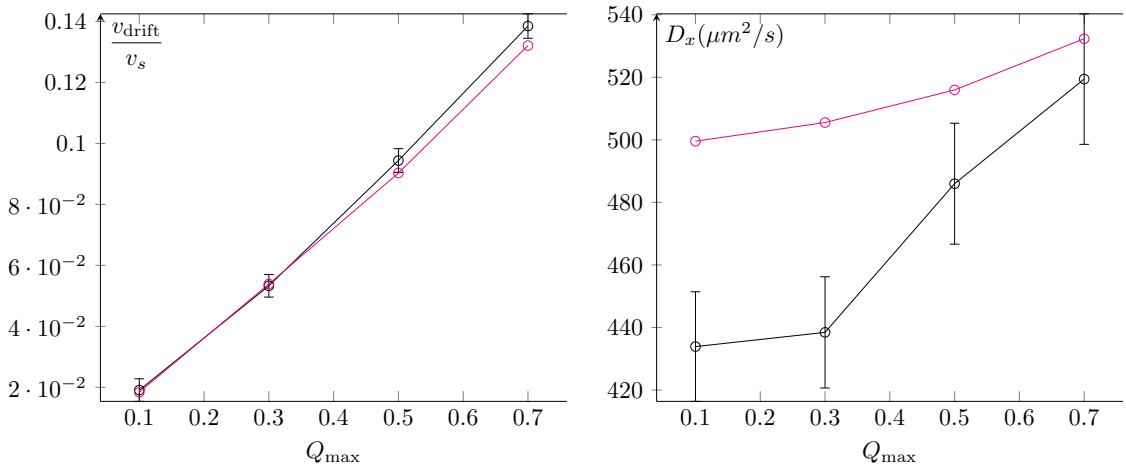

Figure 3.14: Comparison between estimates (3.28) and (3.31) (left) and (3.26) and (3.31) (right) with $\Phi \sim \mathcal{U}[-\alpha, \alpha]$ and $F(Q) = F_4(Q) = \dfrac{1+e^{2Q}}{2}$. The black line is our simulations results and the magenta line is the estimate using p^+ and p^-.

The two estimates for drift velocity agree well, at least for small to moderate level of response, but there is a discrepancy for the motility coefficient for small values of $Q_{\max}$. One possible explanation for this, might be that the p^+, p^- assumption, doesn't weigh in a reduced effect to run times in cases of lower gradient sensed. In other words, a cell swimming in the $(1,0)$ direction is not distinguished from one swimming in the $(1,1)$ direction, for which the intake would be lower. The same trends are observed in other modeling options that are omitted (for $F(Q)$ model or Φ distribution). An illustration of this argument is given in Figure 3.15, which is a radial histogram of the run times of a simulated population in the attractant concentration gradient $\nabla C = (c_1, 0)$.

3.5 Conclusions

In this chapter, we used kernel response models in numerical simulations to explore the changes in chemotactic drift velocity and random motility of cells. In particular, we focused on the outcomes for strong responses, beyond the range of weak response asymptotic results, and different models for the relation between mean run time and cell response $Q(t)$.

The kernel models fall into two basic classes: those with a slow initial response to a sudden increase in attractant $C(t)$, corresponding to the experiments in [49] for changes in run time for a pulse attractant [14]; and those with a rapid initial response [17,37,68]. The asymptotic results for v_{drift} in both models have the same basic features that $\dfrac{v_{\text{drift}}}{v_s}$ is optimal when $\lambda\tau_0 = \mathcal{O}(1)$ or $t_a = \mathcal{O}(\tau_0)$. Both models predict no change in random motility with chemotaxis in an chemoattractant concentration gradient.

Recent experiments have shown that $\frac{v_{\text{drift}}}{v_s}$ can reach up to $0.2 - 0.25$ and reaching these values with these linear models requires large values of $Q_{\max}$, the response level for sustained swimming in the direction of linearly increasing C. Even so, values of $\frac{v_{\text{drift}}}{v_s}$ in our simulations reach 0.15. Also, for strong responses (high $Q_{\max}$), there are significant changes in random motility in a linear gradient in one dimension from the default diffusion of cells swimming in no chemical gradient and the dispersion is not isotropic, as D_x increases more than D_y.

The response $Q(t)$ to changes in attractant levels captures cell excitation and adaptation. We considered the relation $\tau = \tau_0 F(Q)$ separately and evaluated different models beyond the usual linear change in tumble rate $\lambda = \lambda_0 (1 - Q)$ that corresponds to our $F_2(Q) : \frac{1}{\tau} = \frac{1}{\tau_0}(1 - Q)$. Larger values of $\frac{v_{\text{drift}}}{v_s}$ resulted from models F_2 and F_4 that were more asymmetrical compared to F_1 and F_3, which yielded lower drift. The model F_5, which assumes no reduction in run time when swimming down the gradient, as proposed by [48] and suggested by Berg, gives substantially lower drift and larger changes in D_x, D_y. Overall, some reduction in τ below the baseline τ_0 is necessary for efficient chemotaxis, even if it not large compared to potential increases. These estimates for drift and motility neglect the effect of finite duration of tumble intervals, which act to reduce the mean effective drift and dispersion.

It is generally accepted that there is a nonlinear chemotactic sensing mechanism by the chemoreceptors and a nonlinear relation to the cell activation levels. This is explored in Chapter 4. The kernel models we used here may be considered as local linearizations for small gradients of attractant concentration relative to some ambient level. The sensitivity of the response is set by the parameters β_1 and b that control the value of $Q_{\max}$. By focusing on specific values of $Q_{\max}$, we avoid the specific issues of sensitivity and magnitude of the gradient ∇C.

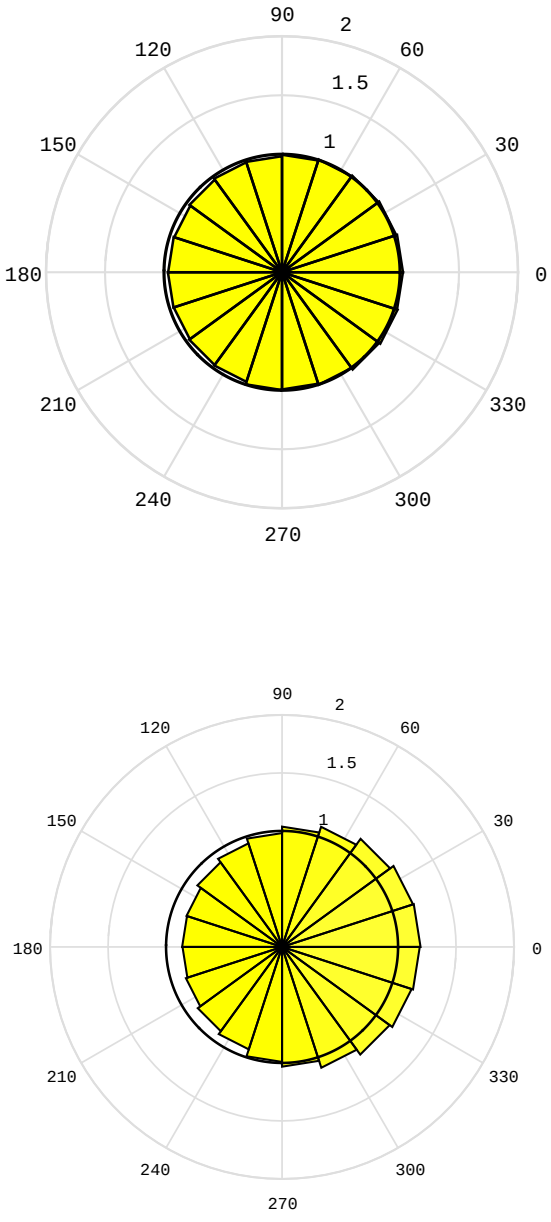

Figure 3.15: Radial histograms of run times per direction in the concentration profile $C(x, y) = c_1 x + c_0$. The simulation parameters are as in Table 3.2 and $\Phi \sim f_\Phi, F(Q) = F_4(Q)$ and $Q_{\max} = 0.1$ (top); $Q_{\max} = 0.5$ (bottom). The black circle represents the baseline runtime $\tau_0 = 1s$.

Chapter 4

Modeling Chemosensing of E. Coli

At the end of Chapter 3, we highlighted the need for a new kind of models to be able to capture stronger responses. With the advancement of imaging technology, in particular Fluorescence Resonance Energy Transfer (FRET) studies, we have been able to specify some details of the sequence of interactions between proteins linking the ligand binding on the chemoreceptors to the rotary motor switching.

In this chapter we describe several reduced mean-field models that have been developed recently and evaluate the chemotactic response they generate. These models are generally more detailed than the ones in Chapter 3 and follow the chemotactic signaling pathway in terms of the CheA kinase activity $a(t)$, the methylation level of the receptor $m(t)$, the concentration of phosphorylated CheY-P $[Y_p](t)$ and finally, the switching rates of the motor. As experimental measurements based on FRET microscopy have progressed, more of the key reaction steps have been quantified and the processes are better known. Refer to Figure 1.2 for an illustration of well-known processes. However, there are several aspects that remain to be quantified reliably, so we avoid the full mean-field pathway models that would simply introduce too many uncertain parameters. Information from the detailed pathway models and from the full mean-field models do provide background context and some of this is noted.

4.1 Reduced Mean-Field Models

The reduced mean-field models aim to utilize the chemotaxis pathway rather than extract an aggregated response like the kernel models of Chapter 3. Each subsection refers to one step of the model relating to one part of the chemical procedure from ligand binding to motor switching.

4.1.1 Mean Receptor Activity

The kinase CheA activity characterizes the sensitivity of the methyl-accepting chemotaxis protein (MCP) receptors that receive extracellular signals. Even though not considered in the previous chapter, the receptors of bacteria cells are concentrated in one of the cell poles, while the motors are gathered in the other [39]. This localization supports the hypothesis of receptor co-operativity for signal amplification: the activity (or inactivity) of one receptor affects the state of neighboring receptors. Ising models have been proposed to model this interaction between individual receptors [7, 21]. Alternatively, we focus on the Monod-Wyman-Changeux Model (MWC), that groups receptors in clusters for concise and faster calculations [42]. The receptor is usually considered to include the tightly bound enzymes CheW and CheA. In its active state, CheA can auto-phosphorylate to form CheA-P which transfers the phosphor group to the freely diffusing CheY protein to form CheY-P. In turn CheY-P binds to the FliM motor proteins and promotes switching, which for E. coli leads to a run to tumble event. The binding of an attractant ligand reduced the activity of CheA and thus leads to a lower rate of switching and longer run times. Because of their connection, $a(t)$ will signify both the receptor and the kinase activity interchangeably, and take values in $(0, 1)$. In the absence of stimuli, activity is at the temperature-dependent equilibrium value a_0: $a_0 = 0.5$ at 32℃ and $a_0 = 1/3$ at 22℃ [51]. Each equilibrium value corresponds to relevant environments: the natural habitat of E. coli is human intestines (32℃) and most experiments are conducted in room temperature (22℃).

The standard model for this first step is relatively well-established [59]. In the presence of ligand in concentration C in the surroundings of the cell, the molecules can bind externally to the MCP receptor proteins. The proteins are assumed to be arranged in clusters of $N = 6$ receptor dimers that act cooperatively. The Monod-Wyman-Changeux (MWC) model expresses the average activity of the receptors as

$$a = \left(1 + \exp\left\{NF(m, C)\right\}\right)^{-1} \tag{4.1}$$

where m is the average receptors methylation level and $F(m, C)$ is the overall free-energy difference given by [40, 54]

$$F(m, C) = f_m(m) + f_L(C) \tag{4.2}$$

$$f_L(C) = \ln\left(\frac{1 + \dfrac{C}{K_i}}{1 + \dfrac{C}{K_a}}\right) \tag{4.3}$$

where K_a, K_i are the ligand dissociation constants to active and inactive receptors respectively

and $f_m(m)$ is the methylation-dependent free-energy difference [63]

$$f_m(m) = \alpha\,(m_0 - m) \tag{4.4}$$

The values of the parameters in the MWC model for bacterial chemotaxis have been experimentally measured [54, 59]. Mean activity a takes values in $(0, 1)$. We focus on the case with $a_0 = 0.5$. At steady state, when no difference in attractant concentration is detected, CheA activity returns to the equilibrium value a_0, such that $F(m, C) = 0$.

The free-energy difference at equilibrium at 32℃ is zero, so the equilibrium methylation level m_c can be computed in terms of the attractant concentration C :

$$\alpha\,(m_c - m_0) = \ln\left(\frac{1 + \dfrac{C}{K_i}}{1 + \dfrac{C}{K_a}}\right) \tag{4.5}$$

$$\Rightarrow m_c = m_0 + \frac{1}{\alpha}\ln\left(\frac{1 + \dfrac{C}{K_i}}{1 + \dfrac{C}{K_a}}\right) \tag{4.6}$$

This is an increasing function with an approximately linear change with $\ln C$ in the range $K_i < C < K_a$, as shown in Figure 4.1.

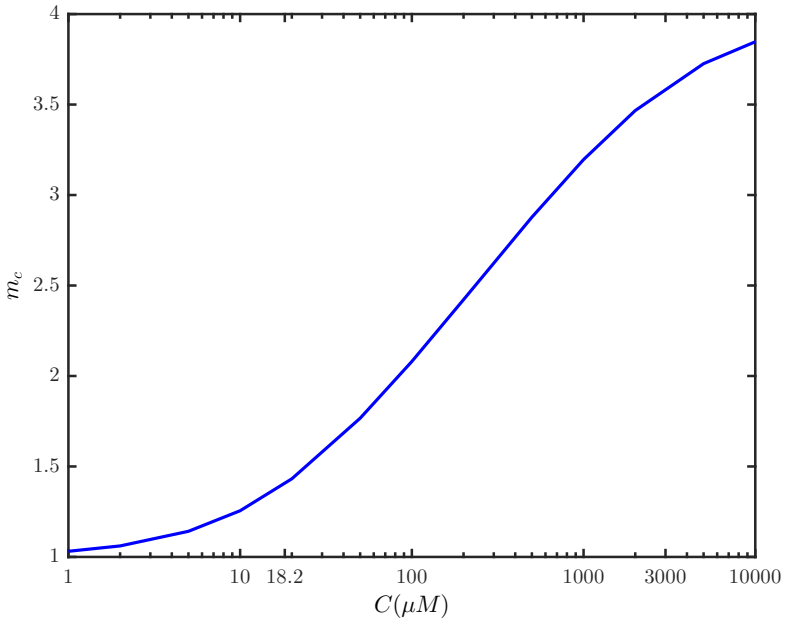

Figure 4.1: Logscale plot of the equilibrium methylation values m_c for different levels of attractant concentration when $a_0 = 0.5$.

4.1.2 Methylation Kinetics

The methylation process resets the receptors slowly to adapt to longer term changes in attractant concentration. The adaptation of the methyl accepting proteins (MCP) to longer term changes in ligand concentration is characterized by the average methylation level $m(t)$.

Many of the recent experiments expose bacterial cells to significant step changes that require a long time for adaptation, on the order of minutes, while chemotactic sensing typically involves smaller changes on the time scale of seconds, in the same magnitude as the average run times and tumble intervals. Every cluster of Tar receptors can have $0-4$ bound sites, therefore, ignoring serine receptors (Tsr), the mean methylation level takes values in $[0, 4]$.

Tu, Shimizu and Berg developed the first reduced pathway model that has become the starting point of subsequent models [61]. The net methylation rate is modeled as a function depending strongly on activity a and only weakly on C, so that

$$\frac{\mathrm{d}m}{\mathrm{d}t} = S(a, m, C) \sim S(a) \tag{4.7}$$

where the dependence on current methylation level is accounted for by the dependence of a on m in Section 4.1.1. This assumption is justified by almost perfect adaptation observed in experiments.

In [61], they further examine the response to an exponential ramp of attractant concentration $C = C_0 \exp(rt)$ in the operational range of $K_i < C < K_a$, where the receptors are not saturated and are able to pick up the signal. In the long term, activity level a adapts to a new equilibrium value from the value with no ligand, a_c. At this new equilibrium point, $\frac{\mathrm{d}a}{\mathrm{d}t} = 0$, so

$$-\frac{N \exp\{N(f_m + f_L)\}}{[1 + \exp\{N(f_m + f_L)\}]^2} \left(-\alpha \frac{\mathrm{d}m}{\mathrm{d}t} + \frac{\mathrm{d}f_L}{\mathrm{d}C}\frac{\mathrm{d}C}{\mathrm{d}t}\right) = 0 \tag{4.8}$$

$$\Rightarrow \left(-\alpha \frac{\mathrm{d}m}{\mathrm{d}t} + \frac{\mathrm{d}f_L}{\mathrm{d}C}\frac{\mathrm{d}C}{\mathrm{d}t}\right) = 0 \tag{4.9}$$

but

$$\frac{\mathrm{d}f_L}{\mathrm{d}C} = \frac{1}{K_i + C} - \frac{1}{K_a + C} \approx \frac{1}{C} \tag{4.10}$$

$$\frac{\mathrm{d}C}{\mathrm{d}t} = rC \tag{4.11}$$

where the approximation on the first line is valid for $K_i \ll K_a$ and $K_i < C < K_a$. Then (4.9) gives

$$\frac{\mathrm{d}m}{\mathrm{d}t} = S(a_c) = \frac{r}{\alpha} \tag{4.12}$$

which is how we can trace out $S(a_c)$ by varying r.

We assume a linear form of $S(a) = k_R(1-a) + k_B a$ as in [30,70], that is the Barkai-Leibler near-perfect adaptation. Other models assume nonlinear forms of $S(a)$, to capture the different adaptation scales between active and inactive receptors [18,61].

4.1.3 Concentration of CheY-P

The next step on the chemotactic response pathway links the activity of the receptors to the levels of phosphorylated CheY protein, CheY-P. When the kinase is active, it auto-phosphorylates to form CheA-P, that transfers the phosphor group to available CheY and CheY-P is formed. Other effects on the concentration of CheY-P in the cytoplasm are auto-phosphorylation and dephosphorylation, and dephosphorylation by CheZ [64]. Total concentration levels of the main enzymes in the chemotaxis pathway, namely CheA, CheY, CheR, CheB and CheZ in Figure 1.2, as well as reaction and decay rates related to the respective processes are given by [18,23,54,64] and references therein. The total concentration of CheA, including its phosphorylated form, is in the range of $5 - 5.3\mu M$, while there is a larger total CheY concentration, reported either at $9.7\mu M$ [18,23] or $18\mu M$ [54,64]. CheY and CheY-P is not localized in a specific area of the cell, rather it diffuses freely with an average diffusivity of $4.6 \pm 0.8\mu m^2 s^{-1}$ [19].

For the models we use in our simulations [30,70], the concentration of CheY-P is assumed to be proportional to activity a, so that $[Y_p](t) = \beta a(t)$, even though nonlinear effects have been observed [63,64]. The proportionality constant β has to be fitted for the specific bacterium modeled and is taken to be $5.8\mu M$ for E. coli [70].

4.1.4 Motor Switch Rates

The level of CheY-P that reaches the cell's rotary motors, $[Y_p]$, determines the switching rates CCW→CW and CW→CCW. For E. coli, higher $[Y_p]$ promotes the switch from CCW rotation (running) to CW rotation (tumbling). When there is ligand bound on the receptors, the activity is decreased, so less $[Y_p]$ is formed and switching to tumbling is suppressed.

In 2000, Cluzel et al. measured the CW bias, the fraction of time spent in CW rotation, and the switching frequency of tethered E. coli cells together with information on the levels of CheY-P present in the cells using fluorescence correlation microscopy [19]. They found that the CW bias versus $[Y_p]$ is fitted by a Hill function for CW bias values between 0.1 and 0.9 with a steep increase starting at $[Y_p] \sim 2\mu M$ and motors remained in the CW state for concentrations higher than $4.6\mu M$. The fitted Hill exponent is 10.3 ± 1.1 with a dissociation constant $K_M = 3.1\mu M$. The switching rate was peaked strongly around $[Y_p] = 3\mu M$, about the same concentration where CW bias is 0.5.

There are two related modeling approaches in determining the switch rates given the CheY-P concentration. One is using directly the Hill function fitted to the experimental results in [19] for the switch rate CCW→CW. The reverse rate CW→CCW can be kept fixed, so that tumble intervals last for a specific brief duration [30]. Alternatively, the CCW and CW states can represent two states in a potential well model with energy barriers that change dynamically with $[Y_p]$ [33,52,60]. This ensures a higher CCW→CW rate when $[Y_p]$ gets large and vice versa. Sneddon, Faeder and Emonet [52] verified that the CW bias resulting from this two-state well model has the proper sigmoidal (Hill's function) form as in [19]. The energy barriers are then $\pm G([Y_p])$ in units of k_BT, where

$$G([Y_p]) = \frac{g_0}{4} - \frac{g_1}{2}\left(\frac{[Y_p]}{K_D + [Y_p]}\right) \tag{4.13}$$

and the transition rates CW→CCW and CCW→CW are

$$k^+ = w_0 \exp\{G([Y_p])/k_BT\} \tag{4.14}$$

$$k^- = w_0 \exp\{-G([Y_p])/k_BT\} \tag{4.15}$$

respectively [70]. The parameters in the definitions (4.13), (4.15) and (4.15) are given values to fit the experimental data in [19]. In particular, $w_0 = 1.3s^{-1}$, $g_0 = g_1 = 40k_BT$ and $K_D = 3.06\mu M$.

4.1.5 Simulation Methods

Similarly to the kernel model of Chapter 3, we set up Monte Carlo simulations of 2D random walks of N number of cells starting at the origin. Supposing that there is a linear gradient $\nabla C = (c_1, 0)$, we measure the drift and motility with the methods presented in Section 3.3.1. For our simulations, we followed two pathway models that differ in the motor switching part described in 4.1.4. In particular, we use the parameters and steps in [30] and [70] in separate runs and compare the outcomes. More details on the implementation and the differences of the two models follow. Zhuang et al. [70] ran experiments with *Serratia marcescens*, a bacterium that runs-and-tumbles like E. coli, and responds in a similar way. Therefore, some of the parameter values used in the model come from measurements in E. coli.

The difference in implementation from the linear kernel models in Chapter 3, is in the calculation of τ that depends on a, m and $[Y_p]$, in place of the coarse-grained term Q. The reorientation bias is modeled in the same way, with several options for the distribution of Φ. Brownian rotation is also added to slightly modify the direction of movement at every timestep. The finite tumble times are built-in through the rate of switching k^+ (or the fixed mean tumble

Algorithm 2 Pseudocode for the 2D random walk : pathway model [70]

for $i = 1, \cdots, N$ **do**
  $(X_{i,1}, Y_{i,1}) \leftarrow (0, 0)$
  $\theta_{i,1} \leftarrow \mathcal{U}[-\pi, \pi]$
  $a \leftarrow {}^1/_2$
  $m \leftarrow 1$
  for $j = 1, \cdots, M-1$ **do**
    $(X_{i,j+1}, Y_{i,j+1}) \leftarrow (X_{i,j}, Y_{i,j}) + \Delta t\, v_s\, (\cos\theta_{i,j}, \sin\theta_{i,j})$
    $F \leftarrow \alpha\,(m_0 - m) + \ln\left({}^{1\,+\,C/K_i}/_{1\,+\,C/K_a}\right)$
    $a \leftarrow [1 + \exp\{NF\}]^{-1}$
    update m
    $[Y_p] \leftarrow \beta a$
    if running **then**
      $k^- \leftarrow w_0 \exp(-G([Y_p]))$
      $\tau \leftarrow {}^1/_{k^-}$
      if rand()$< {}^{dt}/_{\tau}$ **then**
        switch to tumbling
        $\theta_{i,j+1} = \theta_{i,j} + \Phi$
      else
        $\theta_{i,j+1} = \theta_{i,j}$
      end if
    else if tumbling **then**
      $k^+ \leftarrow w_0 \exp(G([Y_p]))$
      $\tau_t \leftarrow {}^1/_{k^+}$
      if rand()$< {}^{dt}/_{\tau_t}$ **then**
        switch to running
      end if
    end if
    $\theta_{i,j+1} = \theta_{i,j+1} + \text{randn}()\sqrt{2D_r\Delta t}$
  end for
end for

time) and we keep track of the mode at each step. The rates k^+, k^- are used to determine the probability of switching between the two modes in a Δt interval as $\Delta t k^+$ and $\Delta t k^-$, assuming a Poisson process. In what follows, we explain the steps in the order of the simulation, according to the pathway stages described in Sections 4.1.1 through 4.1.4.

The model for the receptor activity is standard across mathematical models in the literature [18,30,51,58,61,65,70]. Assuming cooperative binding of ligand C to the receptor complexes of $N = 6$ units, the average activity is given by the MWC model :

$$a = (1 + \exp\{NF(m, C)\})^{-1} \tag{4.16}$$

$$F(m, C) = f_m(m) + f_L(C) \tag{4.17}$$

$$f_m(m) = \alpha\,(m_0 - m) \tag{4.18}$$

$$f_L(C) = \ln\left(\frac{1 + \dfrac{C}{K_i}}{1 + \dfrac{C}{K_a}}\right) \tag{4.19}$$

where $N = 6, \alpha = 1.7, m_0 = 1, K_i = 18.2\mu M, K_a = 3mM$ [40,63].

The methylation dynamics assume the near-perfect adaptation model by Barkai and Leibler [7]. The average methylation level of the receptors $m(t)$ takes values in $(0, 4)$ and satisfies the linear ODE :

$$\frac{\mathrm{d}m}{\mathrm{d}t} = k_R(1-a) - k_B a \tag{4.20}$$

Here, k_R corresponds to the methylation rate of the receptors by the CheR protein and k_B corresponds to the demethylation rate of the receptors by the CheB protein. The two rates are taken to be the same and equal to $0.0033s^{-1}$ [70] or $0.005s^{-1}$ [30] for the equilibrium activity value $a_0 = 0.5$. We tried both values for k_R, k_B in the simulations but, as long as the methylation and demethylation rates remain in that magnitude, the results are not significantly different.

The concentration of CheY-P $[Y_p]$ is proportional to the mean activity $a(t)$, so

$$[Y_p](t) = \beta a(t) \tag{4.21}$$

CheY diffuses freely in the cell and forms CheY-P when it meets the phosphor groups released by CheA. CheA remains localized in the receptor region [39]. The value of the phosphorylation proportionality constant β is fit to data to be $5.8\mu M$.

The last step in the signaling pathway sets the motor switching rates between the two states CCW/CW. We implement two approaches based on [30] and [70].

Kalinin et al. [30] The probability of a switch CCW→CW, or from running to tumbling, in an interval Δt, is $p(a)\Delta t$, where a is the average receptor activity. $p(a)$ is the switch rate that was fitted in [19] as a Hill function with coefficient $H = 10$:

$$p(a) = \frac{1}{\tau_t}\left(\frac{a}{a_{1/2}}\right)^H \tag{4.22}$$

where $a_{1/2}$ is chosen so that in equilibrium, $a = a_0$, the CCW bias is 0.8. In other words, in equilibrium the cells spend 80% of their time in running mode and 20% tumbling, to agree with experimental observations. τ_t is the mean tumble time that doesn't change with the concentration of attractants and $\tau_t = 0.2s$. Solving for $a_{1/2}$: $({}^{a}/_{a_{1/2}})^H = 4 \Rightarrow a_{1/2} = 0.69$. Then the cell is expected to run on average for

$$\tau = \frac{1}{p(a)} \tag{4.23}$$

Even though a mathematical model is presented, [30] is an experimental paper, tracking cells swimming in a microfluidic channel $400\mu m$ wide, where a linear gradient of chemoattractant concentration has been created. By varying the average C and ${}^{\nabla C}/_{C}$, the strongest

chemotactic drift was observed for $\bar{C} = 500\mu M$, where $v_{\text{drift}} = 0.15 - 0.20\, v_s$.

Zhuang et al. [70] Unlike the previous model, both switch rates are modified based on the level of $[Y_p]$. Following the work by [33] and later [60], the transition rates CW→CCW (k^+) and CCW→CW (k^-) are given by a two-state potential model as

$$G([Y_p]) = \frac{g_0}{4} - \frac{g_1}{2}\left(\frac{[Y_p]}{K_D + [Y_p]}\right) \tag{4.24}$$

$$k^+ = w_0 \exp\{G([Y_p])/k_B T\} \tag{4.25}$$

$$k^- = w_0 \exp\{-G([Y_p])/k_B T\} \tag{4.26}$$

where $w_0 = 1.3s^{-1}$, $g_0 = g_1 = 40k_BT$ and $K_D = 3.06\mu M$ are values fitted to data. Specifically, the mean run time is

$$\tau = \frac{1}{k^-} \tag{4.27}$$

where k^- is the switching rate defined in (4.26), assuming Poisson statistics.

The authors experimented on Serratia marcescens that responds similarly to E. coli. They also created linear gradients of ligand concentration in a $500\mu m$ channel. The experiment was in three dimensions but calculations were done with its projection to 2D. Then the average tumble rate up (p^+) and down (p^-) the gradient were statistically estimated to get drift and motility as in [15]. The attractant concentration profiles $\nabla C = \left(\frac{\mathrm{d}C}{\mathrm{d}x}, 0\right)$ ranged from $\frac{\mathrm{d}C}{\mathrm{d}x} = 10^{-3} - 5^{mM/mm}$ with mean concentrations ranging from $5 \times 10^{-3} - 2.5mM$. The strongest chemotactic drift $v_{\text{drift}} = 0.15v_s$ was obtained when $\frac{\mathrm{d}C}{\mathrm{d}x} = 0.2^{mM/mm}$ and $\bar{C} = 0.1mM$.

4.2 Results

The two references we quoted in Section 4.1.5 [30, 70] mention the mathematical models but were mainly experimental. Through our results, we reproduce their outcomes with the simulated bacteria accurately.

4.2.1 Step Change Response

Firstly, we test the response to a step change, assuming that the sensing mechanism is in steady-state at time $t = 0$, when a constant ligand concentration $C = c_0$ is applied. Since the two models only differ in the model for the run time, we present the mean activity and methylation levels $a(t), m(t)$ for both models for increasing step-changes in Figure 4.2. There is an immediate drop in activity, its magnitude depending on the amount of the step change. Then it returns slowly

to its equilibrium value $a_0 = 0.5$. The methylation counteracts the activity and stabilizes on a level higher than $m_0 = 1$, again depending on the magnitude of the change. Refer to Figure 4.3 for higher step changes. The case $c_0 = 0$ corresponds to no change in attractant concentration and yields a constant mean run time equal to $\tau_0 = 1.0062s$ that is compared to the increased run times of positive step-changes.

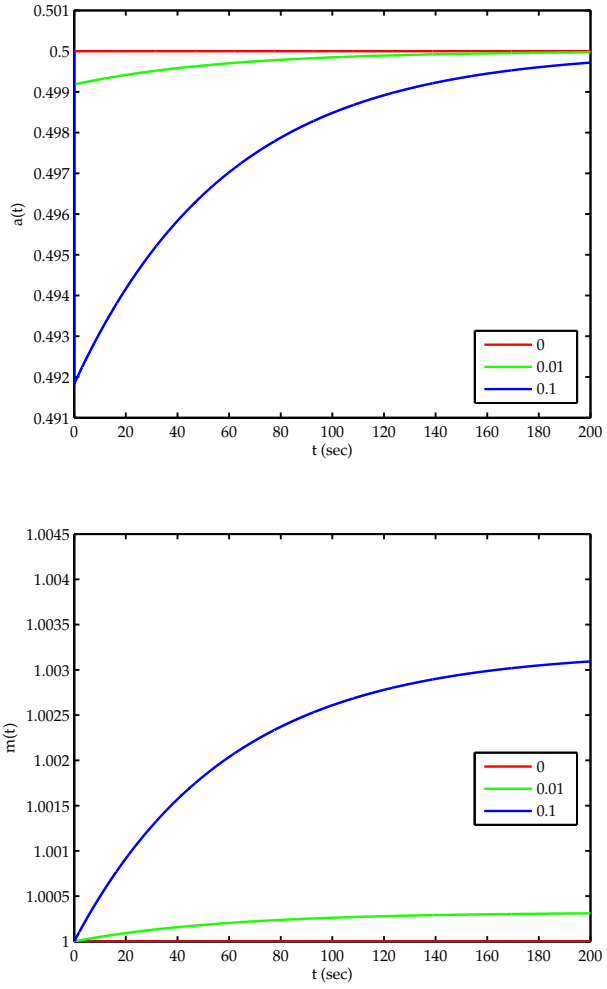

Figure 4.2: The mean receptor activity (top) and methylation (bottom) for a step change $C(t) = c_0\mu M$, according to (4.17) and (4.20). We assume that the system is in steady-state before $t = 0$, so that $a(0) = 0.5$ and $m(0) = 1$. The red line is plotted for reference and corresponds to no change. The green and blue lines correspond to $c_0 = 0.01$ and $c_0 = 0.1$ respectively.

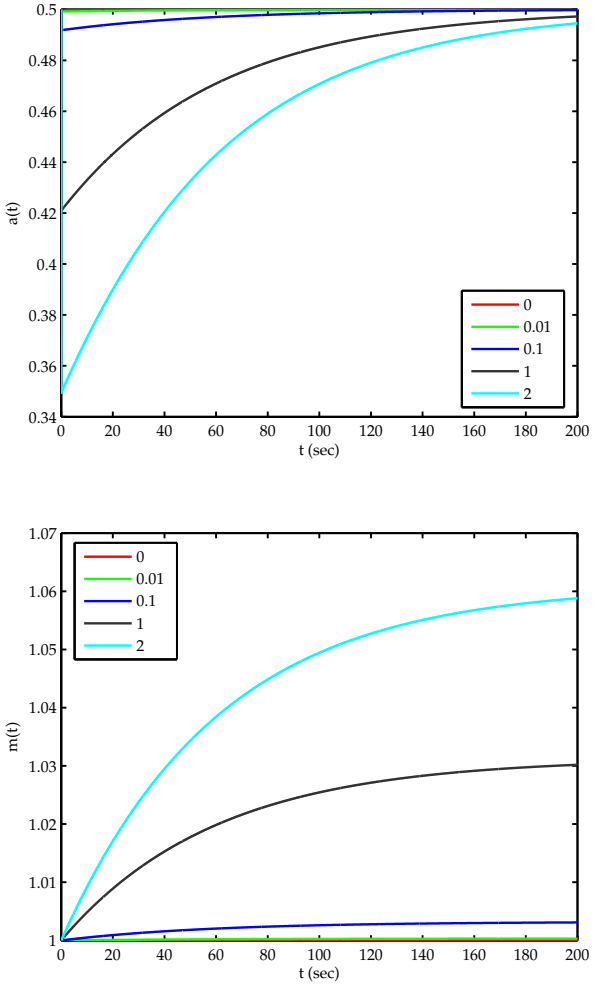

Figure 4.3: The mean receptor activity (top) and methylation (bottom) for a step change $C(t) = c_0\mu M$, according to (4.17) and (4.20). We assume that the system is in steady-state before $t = 0$, so that $a(0) = 0.5$ and $m(0) = 1$. The red line is plotted for reference and corresponds to no change. The green,blue, gray and cyan lines correspond to $c_0 = 0.01$, $c_0 = 0.1$, $c_0 = 1$ and $c_0 = 2$ respectively.

The respective run times based on the two different models in Section 4.1.5 are shown in Figures 4.4 and 4.5. The instantaneous response for Kalinin's model results is weaker for small changes (Figure 4.4) and stronger for a step change of $2\mu M$ (cyan line in Figure 4.5). The run time for a unit step change increases immediately to $\sim 2.4\tau_0$ for both models. Larger step changes, in the order of $10\mu M$ act to eliminate receptor activity completely, leading to unrealistically long run times.

The shape of the run time curves is comparable to that of the kernel models with a rapid initial response [17,37,68] (see Figure 2.4). However, a comparison between kernel and pathway models, is not straightforward, because the nonlinear models of this chapter have several variables in the place of Q, with an implicit relation between them and the mean run time.

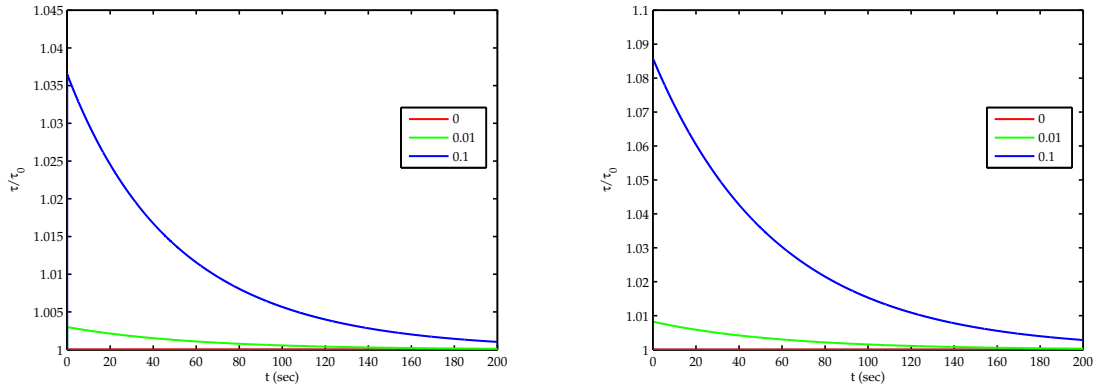

Figure 4.4: The mean run time (normalized by baseline run time τ_0) as it is determined over time through the chemotactic response pathway in the two models : Kalinin et al. [30] (left) and Zhuang et al. [70] (right) for a step change $C(t) = c_0\mu M$, according to (4.23) and (4.27). We assume that the system is in steady-state before $t = 0$, so that $a(0) = 0.5$ and $m(0) = 1$. The red line is plotted for reference and corresponds to no change. The green and blue lines correspond to $c_0 = 0.01$ and $c_0 = 0.1$ respectively.

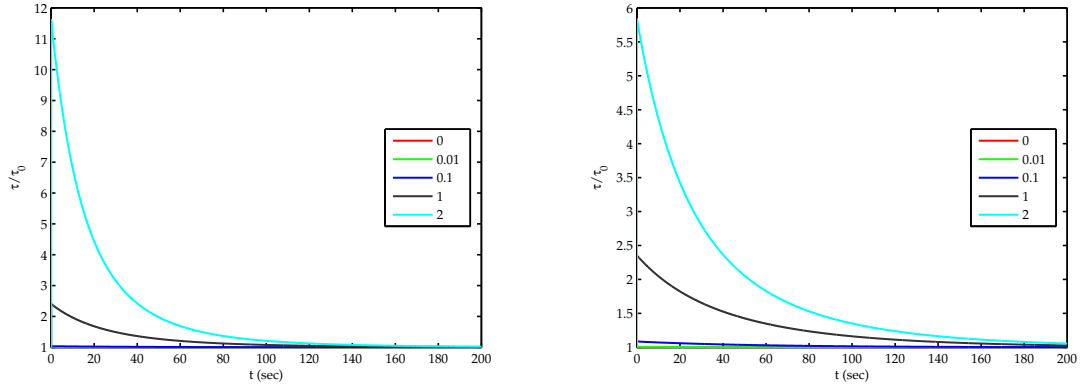

Figure 4.5: The mean run time (normalized by baseline run time τ_0) as it is determined over time through the chemotactic response pathway in the two models : Kalinin et al. [30] (left) and Zhuang et al. [70] (right) for a step change $C(t) = c_0\mu M$, according to (4.23) and (4.27). We assume that the system is in steady-state before $t = 0$, so that $a(0) = 0.5$ and $m(0) = 1$. The red line is plotted for reference and corresponds to no change. The green, blue, gray and cyan lines correspond to $c_0 = 0.01$, $c_0 = 0.1$, $c_0 = 1$ and $c_0 = 2$ respectively.

4.2.2 Comparison to p^+, p^- Approximations

Zhuang et al. used L-aspartate as the chemoattractant and measured the chemotactic drift and motility of the tracked trajectories across a channel with a linear gradient in C using the p^+, p^- approximations introduced in Section 3.4.4 by [15]. Even though the main results focus on the drift velocity, there is mention of the motility coefficient in the supplemental material and it is claimed that this remains on the same levels across the linear gradients of the experiments. We estimate the drift and motility using the methods in Section 3.3.1 that produced different results for stronger responses, like with the kernel models in Section 3.4.4.

This chemosensory model responds to concentration gradients in a wide range, from $0.01mM/mm$ to $1mM/mm$, in agreement to the experiment in [70]. Even though the two estimates agree at some of the points, there is a large difference where the response is stronger. This could be attributed to the fact that the estimate (3.31) is asymptotic and assumes a weak response. See Figures 4.6 and 4.7 for estimates of drift velocity and random motility, in comparison to the p^+, p^- estimates.

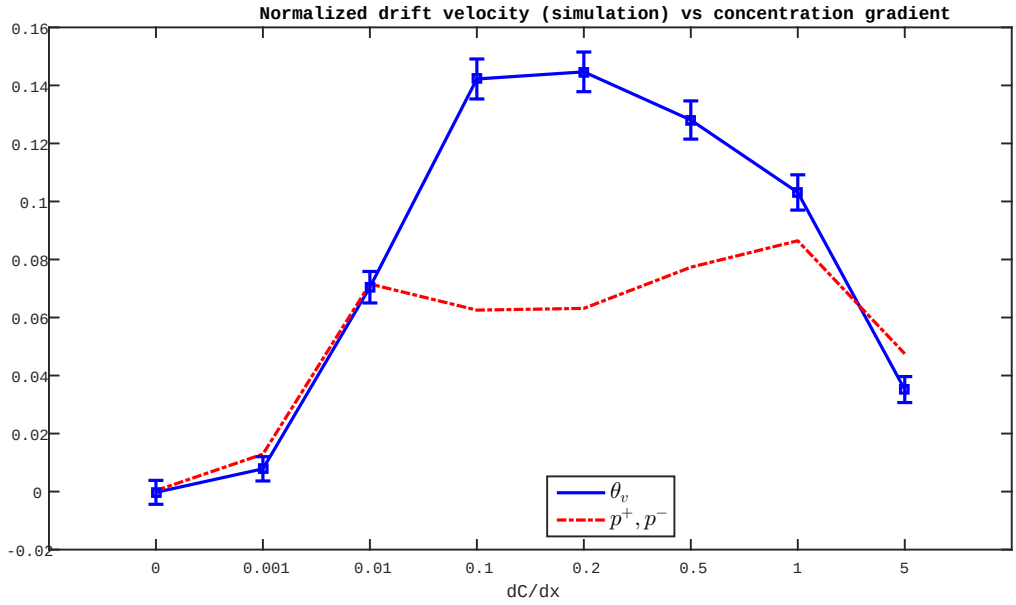

Figure 4.6: The drift velocity estimates (blue line) versus chemoattractant gradient. Compare to the estimates given by (3.31) on the same data (red dashed line). The strongest chemotactic drift is achieved when $\frac{\mathrm{d}C}{\mathrm{d}x} = 0.2mM/mm$ and it is close to $0.15v_s$.

Also, the nonlinear response models of this Chapter are capable of higher drift and substantially higher random motility compared to the linear kernel models of Chapter 3. In particular, for an attractant gradient close to $0.1 - 0.2mM/mm$, we estimate a strong drift, equal to 15% of the swimming speed, corresponding to the high $Q_{\max}$ cases for a reduced kernel model. The random motility is also increased in that range, and is significantly different from the levels of dispersion with the kernel models. Nonlinearity in the signaling process through co-operative binding can be a reason for larger diffusion in that range of concentration gradient, aiming for the organism's ability to explore its environment as much as possible. The simulation results also support our comments in the conclusion of Chapter 3, that shortening runs to the wrong direction is essential for efficient chemotaxis. As shown in Figure 4.8, the run times from the pathway models are indeed shortened in the negative x direction in our setup, for any gradient that yields a drift velocity, making this feature built-in to the internal dynamics. Lastly, the nonlinear models directly include finite tumble intervals, either through a fixed τ_t [30] or a

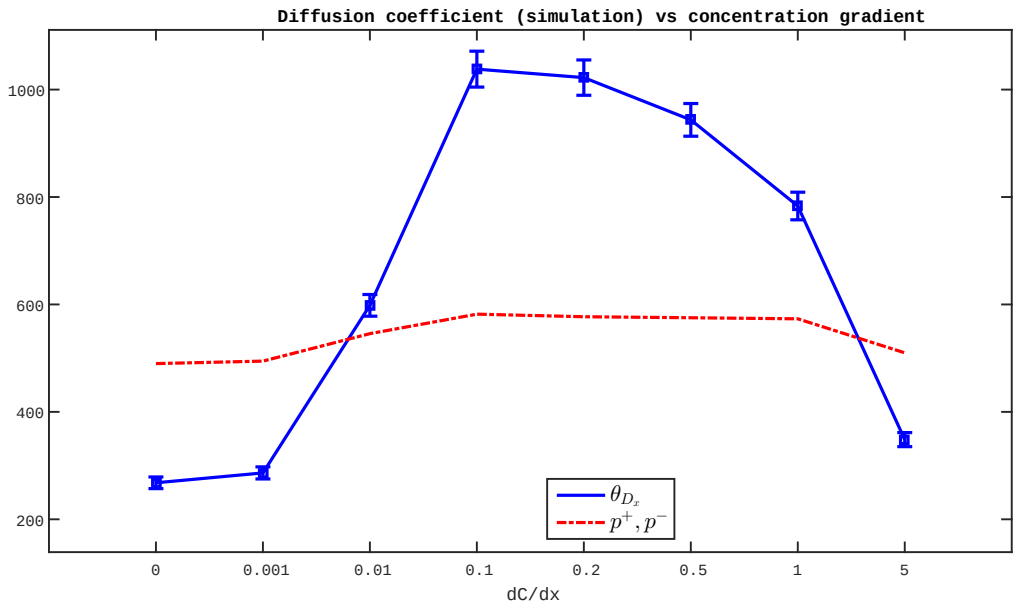

Figure 4.7: The motility coefficient estimates (blue line) versus chemoattractant gradient. Compare to the estimates given by (3.30) on the same data (red dashed line). Contrary to outcomes of the p^+, p^- approximation, motility depends on the ligand concentration gradient.

variable CW→CCW switch rate k^- [70].

4.3 Conclusions

In this chapter, we used nonlinear pathway models in numerical simulations of the chemotactic response of E. coli cells. The motivation for models other than the linear kernel models in Chapter 3 were experimental results with stronger responses than the kernel models could explain [3, 30, 70].

While the kernel models represented the excitation and adaptation stages of the chemoreceptors to a change in the ligand concentration as a coarse term Q, the pathway models introduce more variables corresponding to elements of the sensing mechanism. At the initial stage of excitation, activity of the receptors (and kinase CheA) is reduced, so that tumbles are suppressed, until the receptors return gradually to a normal state, because of the slowly-changing methylation level.

Even though we adopted mean field models for the average receptor activity and methylation level, we observe the expected dynamics in response to step changes: activity is immediately reduced, so that less CheY-P is formed and tumbles happen less often. In the long run, activity returns to its equilibrium value, modeling the mechanism's adaptation. Methylation levels are increased to a higher equilibrium value, as expected from (4.6). The nonlinear models are capable of stronger chemotaxis, due to the high sensitivity of the receptor activity to the attractant

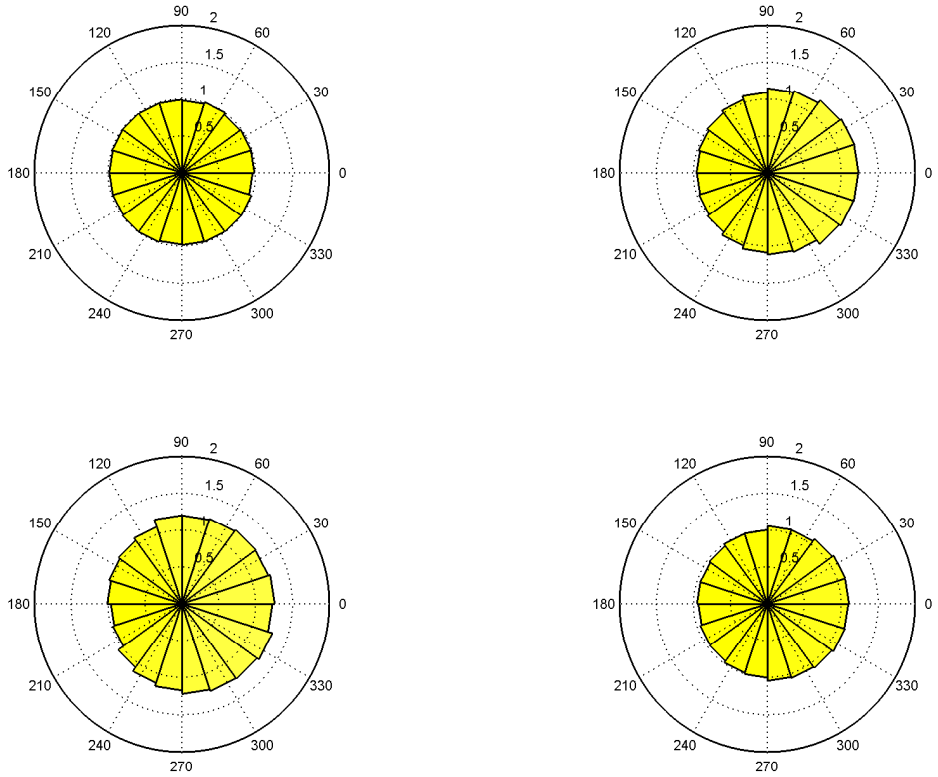

Figure 4.8: Radial histograms of run times per direction in a 2D chemoattractant gradient $\nabla C = (c_0, 0)$ for $c_0 = 0$ (upper left), $c_0 = 0.01mM/mm$ (upper right), $c_0 = 0.2mM/mm$ (lower left) and $c_0 = 5mM/mm$ (lower right). The length of each bar shows the mean run time in the respective direction. In the absence of gradient (upper left), there is no preference in direction. In a linear gradient, run times to the positive x direction $\theta \in \left(-\frac{\pi}{2}, \frac{\pi}{2}\right)$ get longer, and run times to the negative x direction $\theta \in \left(-\pi, -\frac{\pi}{2}\right) \cup \left(\frac{\pi}{2}, \pi\right)$ are shortened. The strongest response is obtained for $c_0 = 0.2mM/mm$ (lower left), when positive runs are increased the most.

concentration and to the steep change in motor switching with the levels of CheY-P [19].

We find that the motility coefficient D_x varies significantly with the concentration gradient. To our knowledge, this is not addressed yet in the relevant literature, or it is found to be almost constant. That could be attributed to the usage of the approximation by [16], that only considers D_x and not D_y, and doesn't take into account the differences in sensed concentration in cells facing to the positive x direction.

Recent studies have quantified some of the reaction rates of auto-phosphorylation, dephosphorylation, methylation etc. [18, 23, 54, 64] but we still don't have complete information to describe the signaling process in full detail. The mean-field models capture the main features of a chemotactic response and explain strong chemotactic drift recorded in vitro. When reliable information on parameters in a more detailed pathway model is known [12, 67], it will be interesting to revisit the models presented in this chapter and modify them accordingly.

Chapter 5

Modeling Chemotactic Response of the Caulobacter Crescentus

Many bacteria have a single flagellum for propulsion, in contrast to the multiple flagella of E. coli. With the reversal of the flagellum motor, the cell traces backwards its previous path for some distance until the motor reverses again. While there may be some slow reorientation of the cell motion by Brownian rotation there would at first appear to be no mechanism for a change in direction or for an efficient chemotactic search. Recent studies have shown that a broad class of uni-flagellated bacteria execute a "run–reverse–flick" motion, whereby the cell changes direction as the motor switches from reverse to run mode [66]. In 2013, Stocker at al. further identified the physical details of the flick and related it to a buckling of the flexible coupling between the motor and the flagellum, as this goes from tension to compression with the change of direction [53].

Among the bacteria that exhibit this motion is the marine bacterium *Vibrio alginolyticus* (or simply Vibrio) [66]. The average cell body is 3.2 μm long with mean flagellum length of 4.6 μm, and mean swim speed of $47 \mu m/s$. The mean run time is shorter than E. coli, measured at about $0.5s$ [53]. Similar to the reorientation of E. coli after a tumbling phase, the observation is that there is an angle bias with the flick concentrated around 90 deg [66]. Other marine bacteria have been seen to exhibit similar modes of swimming and the characteristics of their chemotaxis are reviewed in [56].

Even though not all details of the E. coli biochemical pathway is known, in comparison, the response of single flagellum cells is still being explored and there are many unanswered questions [57]. However, Vibrio is becoming a prototype bacterium for the study of chemotaxis in such cells [6, 66, 69]. Xie et al. measured the switching rates k_f from a forward run (CCW) to a reverse run (CW) and k_b from a reverse run (CW) to a forward run (CCW) for these cells,

in response to small step changes in chemoattractant (in this case, serine) [66]. In steady state, $k_{f,0} = 2.3s^{-1}$ and $k_{f,0} = 1.9s^{-1}$. In general, a more substantial change in k_f is observed than in k_b, a behavior similar to E. coli, where runs up a concentration gradient are significantly increased, while runs down the gradient are moderately decreased.

Another monotrichous bacterium exhibiting the "run–reverse–flick" pattern is the *Caulobacter crescentus* (or simply Caulobacter) that is studied by Professor J. Tang's group in Physics at Brown University. This cell, typically found in groundwater, has different stages in its development – a swarmer cell that is motile, driven by a single polar flagellum and a stalked cell that attaches to a surface and sheds its flagellum. The stalked cell will divide over $20 - 30$ minutes to generate a new swarmer cell. Experiments require the synchronization of the cells to give a working population of swarmer cells. Morse et al. [43] measured the response of these cells to a concentration gradient of oxygen or aerotaxis using a micro-channel flow device similar to that by [3]. Aerotaxis differs in that oxygen moves freely across the cell membrane and there is no specific MCP receptor. There is a metabolic effect within near-membrane cell mitrochondria, where ATP is generated. Morse et al. further note that the average swimming speed is $40\mu m/s$ and the average run times (forward or reverse) are between $1 - 2$ seconds. With or without aerotaxis, the mean duration of a reverse run is $1.3s$, while the forward run time averages $1.85s$, increasing by 30% at higher oxygen levels while only decreasing by 10% at corresponding lower oxygen concentrations.

In this chapter, the aim is to give a baseline study for the chemotactic response of a uniflagellated swimmer using the existing kernel-based models studied earlier in Chapter 3. The question is whether this simple model would give a significant chemotactic response or whether one should postulate that both the durations of forward runs and reverse runs are modulated. Experimental data suggests that in chemical gradients, average reverse times remain practically constant and it is the average forward runs duration that is significantly modified [45].

5.1 A Kernel Model

Our approach for modeling the run-reverse-flick strategy of the Caulobacter is to use a kernel-type model as with E. Coli for the forward run times and keep a fixed reverse run time, when the cell changes swimming mode. This allows us to compare the dynamics between the two strategies of run-reverse-flick and run-and-tumble.

Just like E. Coli uses a "tumble" to change directions between runs, when transitioning between a reverse and a forward run, the Caulobacter performs a "flick", a sudden change in orientation. The physical interpretation of this move, is that the hook where the flagellum is

attached gets buckled, causing the cell to reorient with a large angle difference [36,43,53]. Recent experiments with the latest sophisticated tracking tools have provided insight into the nature of the flick [66, 69]. Even though the exact distribution of the flick angles seem to depend on the cell size, the trend is that they follow a distribution peaked at and symmetric with respect to $\frac{\pi}{2}$ (Figure 5.1).

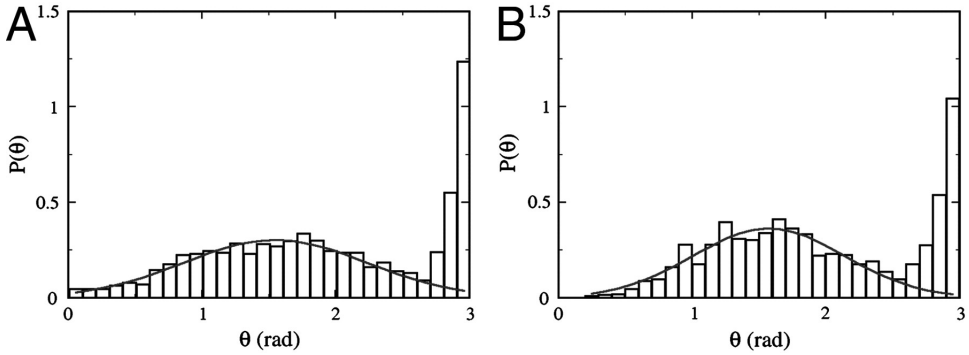

Figure 5.1: Figure 2 in [66]. The sample distribution of flick angles of the Vibrio swimming in a homogeneous medium (left) and in a sharp chemical gradient (right). There are two peaks that the authors attribute to flicks $\left(\text{at } \frac{\pi}{2}\right)$ and reversing from forward to a reverse run (at π). The solid lines are normal distribution fits to the data, ignoring the second peak.

Similar to E.Coli, we assume that the mean forward run time is given by

$$\tau_{\text{fwd}}(t) = \tau_0 F(Q(t)) \tag{5.1}$$

with the same assumptions for $F(Q)$ as in Chapter 3. We still calculate the bias term Q with one of the two models : either (2.6) or (2.11)[1]. Between forward runs, the cells move in the reverse direction for a small duration and that behavior introduces different dynamics from the dynamics of tumbling, i.e. staying on the same spot, not only because the receptors are still receiving signals but also because the bacteria physically backtrack on space they have already covered. We find that a significant factor here is the Brownian motion, because it lets reverse runs diverge from the original path. Figure 5.2 shows a sample run-reverse-flick trajectory.

We assume that the forward and reverse run times follow Poisson statistics, so that the probability of reversing (flicking) in a short interval Δt is $\Delta t/\tau_{\text{fwd}}$ ($\Delta t/\tau_{\text{rev}}$). The mean run time of a forward run may be $\tau \neq \tau_{\text{fwd}}$, in which case the probability of reversing in a short interval Δt is $\Delta t/\tau$. This is to simplify the simulation and explore possible correspondence with E. coli. However, the aerotaxis experiments by Tang et al. suggest that the Caulobacter has multiple CheY proteins that change the dynamics of motor switching from the well-known E. coli response [45]. Indeed, as shown in Figures 5.3, 5.4, 5.5, 5.6 and 5.7, the kernel model doesn't

[1]The simulation results shown are the ones obtained with (2.6). The two models give similar results in this case as well.

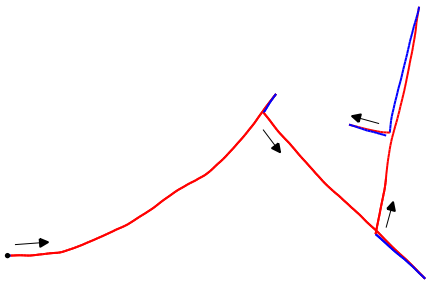

Figure 5.2: A sample trajectory of run-reverse-flick bacterium. The black dot is the starting point and arrows indicate the direction of forward runs. Forward runs are in red and reverse runs in blue. Reverse runs are typically shorter and backtrack to the most recent run for a short duration before flicking and starting a new run.

give the strong chemotactic response of the Vibrio and Caulobacter.

5.1.1 Simulation Methods

To test this simple model for chemotactic efficiency for Caulobacter swimmers, we set up a simulation of N cells performing a 2D random walk starting from the origin. At every time step, we update their location according to the most recent direction of motion and check if they will reverse or flick, depending on whether they are currently forward running or reverse running respectively. In the event of reversing, the direction of movement changes by π (modulo 2π). On the other hand, the flick is modeled by Φ that now follows the normal distribution $\mathcal{N}(\mu = \pi/2, \sigma = \pi/6)$. To illustrate the effect of Brownian rotation, we execute our simulation for $D_r = 0$ and $D_r = 0.062\text{rad}^2/\text{s}$. The rest of the input parameters are reported in Table 5.1.

symbol	meaning	value
N	number of swimmers	8000
T	duration of simulation [s]	50
Δt	timestep of random walk [s]	0.01
τ_{fwd}	baseline mean forward run time [s]	1
v_s	swimming speed [μm]/[s]	30
τ_{rev}	fixed mean reverse run time [s]	1
λ	scaling parameter of model in [14] $[\text{s}]^{-1}$	2
c_1	linear coefficient of concentration function [μM/μm]	0.4
D_r	Brownian rotation coefficient $[\text{rad}]^2/[\text{s}]$	0.062
CL	confidence level	95%

Table 5.1: Input parameters for simulations of the Caulobacter random walk.

Algorithm 3 Pseudocode for the 2D random walk : kernel model for the Caulobacter

for $i = 1, \cdots, N$ **do**
  $(X_{i,1}, Y_{i,1}) \leftarrow (0, 0)$
  $\theta_{i,1} \leftarrow \mathcal{U}[-\pi, \pi]$
  for $j = 1, \cdots, M-1$ **do**
    $(X_{i,j+1}, Y_{i,j+1}) \leftarrow (X_{i,j}, Y_{i,j}) + \Delta t\, v_s\, (\cos\theta_{i,j}, \sin\theta_{i,j})$
    update Q
    if running **then**
      update $\tau = \tau_{\text{fwd}} F(Q)$
      if rand()$< {}^{dt}/_{\tau}$ **then**
        $\theta_{i,j+1} = \theta_{i,j} + \pi$
      else
        $\theta_{i,j+1} = \theta_{i,j}$
      end if
    else
      if rand()$< {}^{dt}/_{\tau_{\text{rev}}}$ **then**
        $\theta_{i,j+1} = \theta_{i,j} + \Phi$
      else
        $\theta_{i,j+1} = \theta_{i,j}$
      end if
    end if
    $\theta_{i,j+1} = \theta_{i,j+1} + \text{randn}()\sqrt{2D_r\Delta t}$
  end for
end for

5.2 Results

The drift velocity and motility coefficient for the different response models $F(Q)$ are shown in Figures 5.3, 5.4, 5.5, 5.6 and 5.7. The black lines come from simulations with no Brownian rotation, while the blue ones correspond to simulations including Brownian rotation. The strongly asymmetrical models $F_2(Q)$ and $F_4(Q)$ result in the highest drift and random motility, $\sim 0.1 v_s$ and $500 \mu m^2/s$ respectively. Even these, however, fall short from actual chemotactic drift of the Vibrio, that reportedly has a threefold larger chemotactic velocity than E. coli [57, 66]. The response models $F_1(Q), F_3(Q)$ produce very low drift ($\sim 0.08 v_s$) and $F_5(Q)$ even more so ($\sim 0.05 v_s$). Most experiments do not provide information on random motility of uniflagellated bacteria, so we don't know how our estimates compare to the baseline random motility.

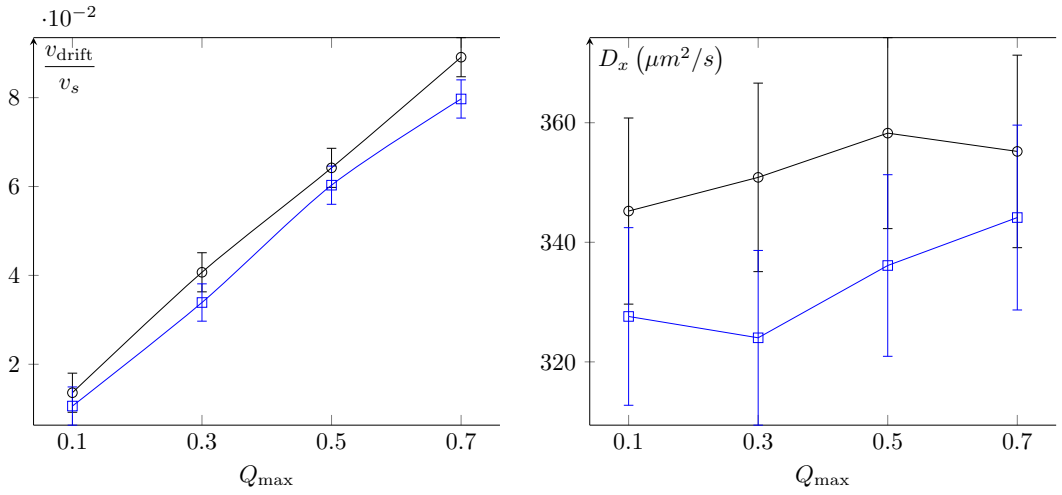

Figure 5.3: Simulation results for a kernel model for the Caulobacter. $\frac{v_{\text{drift}}}{v_s}$(left) and D_x (right) when $F(Q) = F_1(Q) = 1 + Q$. The black (blue) line corresponds to results without (with) Brownian rotation.

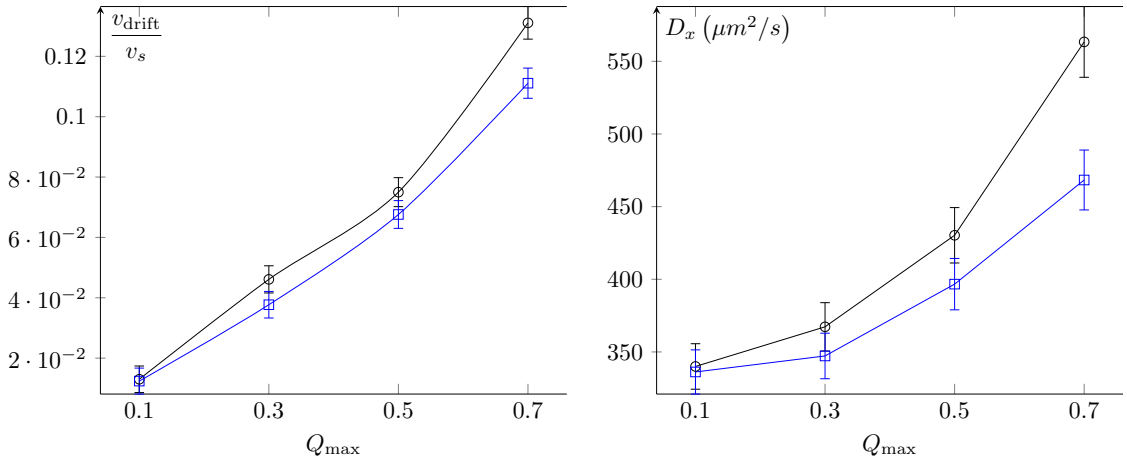

Figure 5.4: Simulation results for a kernel model for the Caulobacter. $\frac{v_{\text{drift}}}{v_s}$(left) and D_x (right) when $F(Q) = F_2(Q) = (1 - Q)^{-1}$. The black (blue) line corresponds to results without (with) Brownian rotation.

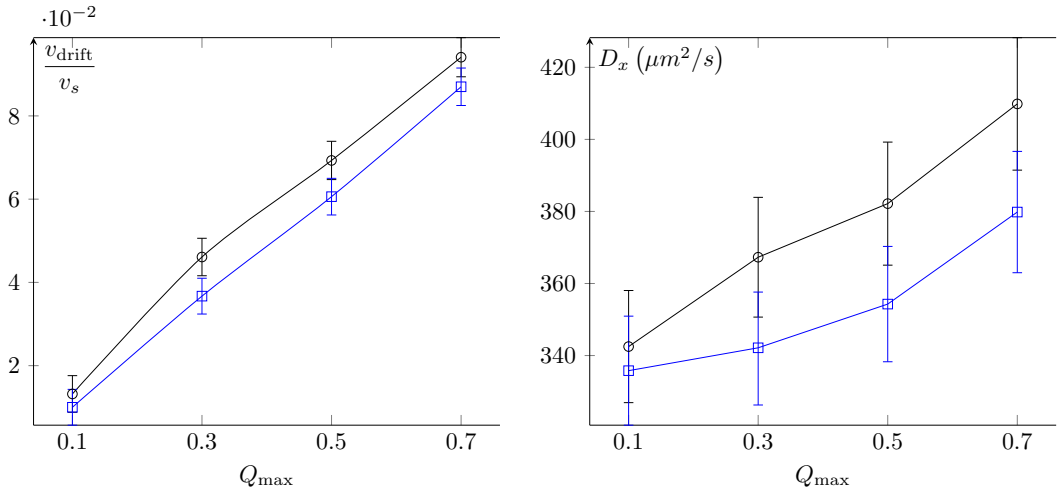

Figure 5.5: Simulation results for a kernel model for the Caulobacter. $\frac{v_{\text{drift}}}{v_s}$(left) and D_x (right) when $F(Q) = F_3(Q) = e^Q$. The black (blue) line corresponds to results without (with) Brownian rotation.

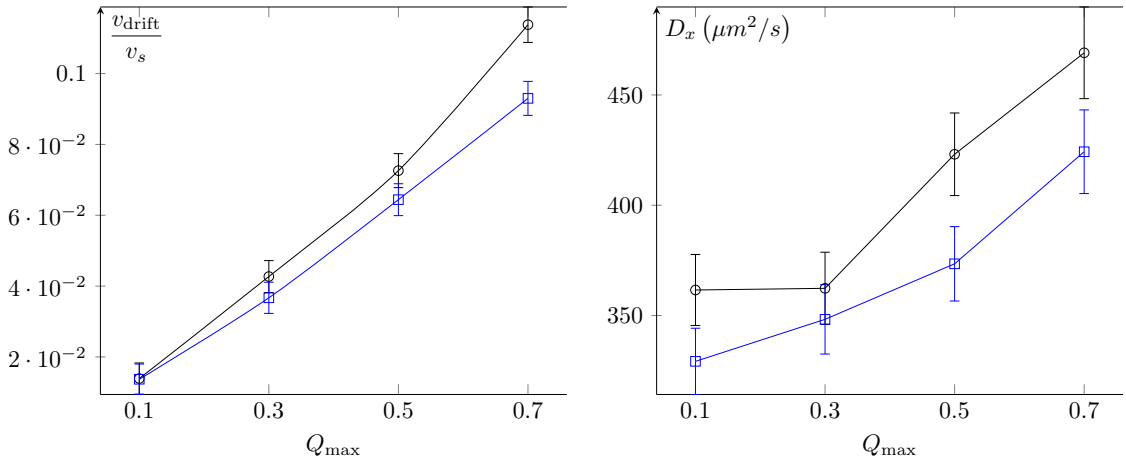

Figure 5.6: Simulation results for a kernel model for the Caulobacter. $\frac{v_{\text{drift}}}{v_s}$(left) and D_x (right) when $F(Q) = F_4(Q) = \frac{1+e^{2Q}}{2}$. The black (blue) line corresponds to results without (with) Brownian rotation.

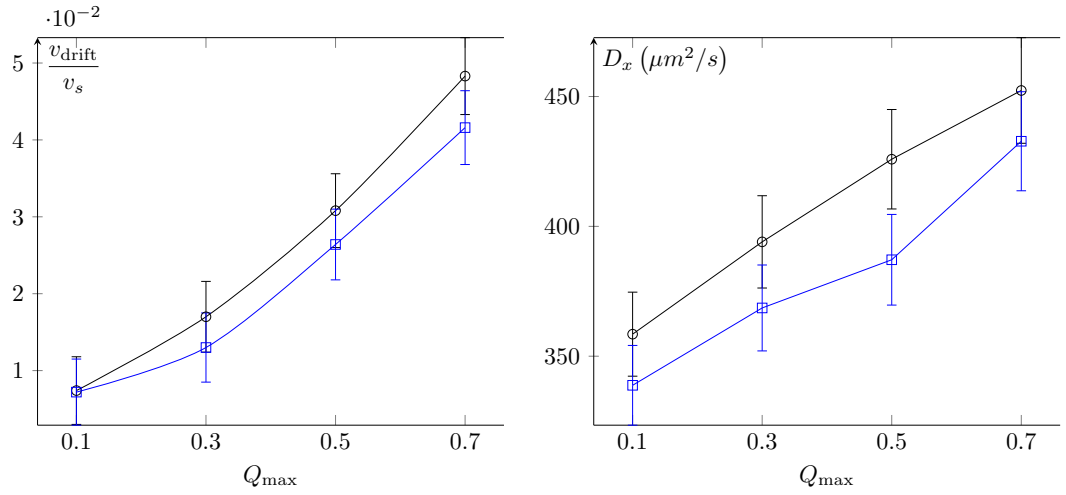

Figure 5.7: Simulation results for a kernel model for the Caulobacter. $\frac{v_{\text{drift}}}{v_s}$(left) and D_x (right) when $F(Q) = F_4(Q) = 1 + Q$ if $Q > 0$; 1 otherwise. The black (blue) line corresponds to results without (with) Brownian rotation.

The results presented here show that the simple model that worked for E. coli is not sufficient to account for the generally strong chemotactic response of the Caulobacter or other uniflagellated bacteria. Further investigation of the modulation of possibly both forward and reverse run times needs to be considered. In addition, adaptation in the two modes, forward and reverse running, might have a different scale of adaptation relative to the average τ_{fwd} and τ_{rev}. In any case, it is likely that a pathway model for the Caulobacter, like the one for E. coli in Chapter 4, will capture the switch rates more accurately.

5.3 Conclusions

In this chapter, we attempted to model the chemotactic response of a uniflagellated bacteria that executes the "run-reverse-flick" strategy with a reduced kernel model. We conclude that such a model is too simple to capture the complexity of this case, and that a pathway model would be more appropriate.

For E. coli, the switch between run and tumbles is viewed as a Poisson process and the statistical distribution of run times is exponential [10]. The mean run time is modulated by the chemotactic response, while the mean tumble interval is essentially constant.

For the Caulobacter crescentus, the forward motion corresponds to a CW rotation of the cell motor and the reverse motion corresponds to CCW rotation [45]. With no stimulus, the CW bias, i.e. the fraction of time the motor is in the CW state, is 0.72, and the distributions for the mean duration of CW and CCW intervals are not simple exponentials, but both have a peak at about $0.7s$. This feature persists with aerotaxis. Tang et al. propose a model for the

switching of the motor based on the rate of binding of CheY-P to the motor's FliM proteins [45]. Further details are given [44]. The structure of this model is similar to that of Zhuang et al. [70] considered in Chapter 4, and does indeed predict a distribution for CW and CCW intervals that is not exponential. In 2008, Tu considered the possibility of such an outcome for motor switching and attributed this to a lack of detailed balance commonly found in Markov processes [58]. Yang et al. postulated that this may be beneficial for a chemotactic strategy of these uniflagellated cells [69].

Overall, modeling the response of the Caulobacter and other uniflagellated bacteria needs to take into account a different set of dynamics, due to its signaling pathway. Even though not intuitively straightforward, both the forward and reverse run time durations need to be controlled.

Chapter 6

Conclusions and Future Directions

In the previous chapters, we considered different levels of mean-field models for the chemotactic response motile bacteria. We have taken the multi-flagellated, peritrichous bacterium E. coli as the reference organism. There is extensive information on the physical structure of these cells, their locomotion and the biochemical pathways within the cell that links the response to ligand binding at the receptors to the change in motor rotation. Our first goal was to identify at what level a realistic model can be constructed that captures the overall response, yet is simple enough to use in future microscopic simulations of cells in nonhomogeneous environments. Detailed models have been proposed that aim to reproduce the full reaction kinetics of all the component enzymes and their relationship to the motor response. These full models may involve up to 100 equations and a large number of reaction rates and kinetic coefficients. Measurements using Forster resonance energy transfer, also known as fluorescent energy transfer (FRET), have made it possible to determine a number of these but most remain poorly characterized. Even when these values are measured, they must often still be tuned within the context of a full model to reproduce observed outcomes. A lower level model avoids the need to specify a large set of parameters.

To this end, we studied the results of kernel-based models that relate the cell activation variable $Q(t)$ to the time history of the local attractant concentration $C(t)$. These were initially based on the experiments of Berg et al [10, 11, 49]. While the standard assumption is that the tumble rate is proportional to $1 - Q$, we have explored other options for what-if scenarios. We examine both chemotactic drift and changes in random motility.

We conclude that these kernel models do not predict the higher values of chemotactic efficiency, $\frac{v_{\text{drift}}}{v_s}$, seen in more recent experiments [3, 30, 70].

We then evaluated the two models by Kalinin et al. [30] and Zhuang et al. [70], that were

based on more details on the signaling pathway of E. coli. Questions remain about the appropriate values of parameters involved, like k_R, k_B for the methylation adaptation. Methylation is a key factor for adaptation to persistent stimuli. Other factors contribute, such as the autodephosphorylation of CheA and CheY, or the action of CheZ and dissociation rates between CheY-P and the FliM proteins of the motors.

The simple kernel models are not appropriate for monotrichous bacteria that "run-reverse-flick". Even though a positive drift and increased motility are obtained, they are far smaller to their real-life counterparts. We need to explore the nonlinear models in the context of motor switching. There is a basic question of how the history of $C(t)$ can be amended, based on forward or reverse runs, and whether other pathways need to be included beyond the standard E. coli dynamics.

In future work, we would examine how these cell-based models may be used to simulate the migration of cells in response to localized sources of attractants where the spatial scales are on the order of mm or less and the time scales are short, on the order of a minute or less. This is relevant to the microscopic world of these organisms, especially in nutrient sparse environments. This context is beyond the scope of PDE models such as the Keller-Segel model that relates to long term evolution of large cell populations on the time scale of hours and larger length scales.

Another possible direction follows up on [64], where the question posed is whether localization of some of the pathway proteins impact the resulting dynamics. Tangent to that direction, we would perform a sensitivity analysis of the pathway model to a few of the reaction rates. These rates have been studied carefully only recently, and estimates for their values vary from reference to reference. Furthermore, they depend on specific environmental conditions, such as temperature, so it is important to figure out their impact on the system and to what extend we can allow for measurement error.

Finally, we would design a Markov chain model for the pathway of the Caulobacter with a fixed transition matrix, according to [45] and similar to the approach in [58]. Eigenvalue analysis or matrix manipulation might give some quantitative or asymptotic outcomes to figure out parts of the pathway. This signaling pathway in uniflagellated bacteria is more complex than E. coli and less details are known.

Bibliography

[1] Julius Adler. Chemotaxis in bacteria. *Science*, 153(3737):708, 1966.

[2] Julius Adler. Effect of amino acids and oxygen on chemotaxis in escherichia coli. *Journal of Bacteriology*, 92(1):121–129, 1966.

[3] T. Ahmed and R. Stocker. Experimental verification of the behavioral foundation of bacterial transport parameters using microfluidics. *Biophys J*, 95(9):4481–93, 2008.

[4] U. Alon, M. G. Surette, N. Barkai, and S. Leibler. Robustness in bacterial chemotaxis. *Nature*, 397(6715):168–171, 1999.

[5] Wolgang Alt. Biased random walk models for chemotaxis and related diffusion approximations. *Journal of Mathematical Biology*, 9(2):147–177, 1980.

[6] Tuba Altindal, Suddhashil Chattopadhyay, and Xiao-Lun Wu. Bacterial chemotaxis in an optical trap. *PLoS ONE*, 6(4):e18231, 2011.

[7] N. Barkai and S. Leibler. Robustness in simple biochemical networks. *Nature*, 387(6636):913–917, 1997.

[8] Howard C. Berg. *Random walks in biology.* Princeton University Press, Princeton, N.J. :, 1983.

[9] Howard C. Berg. Motile behavior of bacteria. *Physics Today*, 53(1):24–29, 2000.

[10] Howard C. Berg and Douglas A. Brown. Chemotaxis in escherichia coli analysed by three-dimensional tracking. *Nature*, 239(5374):500–504, 1972.

[11] Steven M. Block, Jeffrey E. Segall, and Howard C. Berg. Impulse responses in bacterial chemotaxis. *Cell*, 31(1):215–226, 1982.

[12] D. Bray, M. D. Levin, and K. Lipkow. The chemotactic behavior of computer-based surrogate bacteria. *Curr Biol*, 17(1):12–9, 2007.

[13] Douglas A. Brown and Howard C. Berg. Temporal stimulation of chemotaxis in escherichia coli. *Proceedings of the National Academy of Sciences of the United States of America*, 71(4):1388–1392, 1974.

[14] A. Celani and M. Vergassola. Bacterial strategies for chemotaxis response. *Proc Natl Acad Sci U S A*, 107(4):1391–6, 2010.

[15] K. C. Chen, R. M. Ford, and P. T. Cummings. Cell balance equation for chemotactic bacteria with a biphasic tumbling frequency. *J Math Biol*, 47(6):518–46, 2003.

[16] Kevin C. Chen, Peter T. Cummings, and Roseanne M. Ford. Perturbation expansion of alt's cell balance equations reduces to segel's one-dimensional equations for shallow chemoattractant gradients. *SIAM Journal on Applied Mathematics*, 59(1):35–23, 1998.

[17] D. A. Clark and L. C. Grant. The bacterial chemotactic response reflects a compromise between transient and steady-state behavior. *Proc Natl Acad Sci U S A*, 102(26):9150–5, 2005.

[18] Diana Clausznitzer, Olga Oleksiuk, Linda Løvdok, Victor Sourjik, and Robert G. Endres. Chemotactic response and adaptation dynamics in escherichia coli. *PLoS Computational Biology*, 6(5):e1000784, 2010.

[19] Philippe Cluzel, Michael Surette, and Stanislas Leibler. An ultrasensitive bacterial motor revealed by monitoring signaling proteins in single cells. *Science*, 287(5458):1652–1655, 2000.

[20] E. A. Codling, M. J. Plank, and S. Benhamou. Random walk models in biology. *J R Soc Interface*, 5(25):813–34, 2008.

[21] T. A. J. Duke and D. Bray. Heightened sensitivity of a lattice of membrane receptors. *Proceedings of the National Academy of Sciences of the United States of America*, 96(18):10104–10108, 1999.

[22] Michael. Eisenbach. *Chemotaxis*. Imperial College Press ;, London :, 2004.

[23] T. Emonet and P. Cluzel. Relationship between cellular response and behavioral variability in bacterial chemotaxis. *Proc Natl Acad Sci U S A*, 105(9):3304–9, 2008.

[24] S. Fan and R. G. Endres. A minimal model for metabolism-dependent chemotaxis in rhodobacter sphaeroides (dagger). *Interface Focus*, 4(6):20140002, 2014.

[25] Roseanne M. Ford and Peter T. Cummings. On the relationship between cell balance equations for chemotactic cell populations. *SIAM Journal on Applied Mathematics*, 52(5):1426–16, 10 1992. Copyright - Copyright] © 1992 Society for Industrial and Applied Mathematics; Last updated - 2012-07-02.

[26] Desmond J. Higham. Modeling and simulating chemical reactions. *SIAM Review*, 50(2):347–368, 2008.

[27] T. Hillen and K. J. Painter. A user's guide to pde models for chemotaxis. *J Math Biol*, 58(1-2):183–217, 2009.

[28] Berg Howard C. *E. coli in motion*. Springer, New York, 2004.

[29] George A. Jackson. Simulating chemosensory responses of marine microorganisms. *Limnology and Oceanography*, 32(6):1253–1266, 1987.

[30] Y. V. Kalinin, L. Jiang, Y. Tu, and M. Wu. Logarithmic sensing in escherichia coli bacterial chemotaxis. *Biophys J*, 96(6):2439–48, 2009.

[31] P. M. Kareiva and N. Shigesada. Analyzing insect movement as a correlated random walk. *Oecologia*, 56(2/3):234–238, 1983.

[32] Evelyn F. Keller and Lee A. Segel. Model for chemotaxis. *Journal of Theoretical Biology*, 30(2):225–234, 1971.

[33] Shahid Khan and Robert M. Macnab. The steady-state counterclockwise/clockwise ratio of bacterial flagellar motors is regulated by protonmotive force. *Journal of Molecular Biology*, 138(3):563–597, 1980.

[34] Eric Lauga and Thomas R. Powers. The hydrodynamics of swimming microorganisms. *Reports on Progress in Physics*, 72(9):096601, 2009.

[35] Milena D. Lazova, Tanvir Ahmed, Domenico Bellomo, Roman Stocker, and Thomas S. Shimizu. Response rescaling in bacterial chemotaxis. *Proceedings of the National Academy of Sciences of the United States of America*, 108(33):13870–13875, 2011.

[36] B. Liu, M. Gulino, M. Morse, J. X. Tang, T. R. Powers, and K. S. Breuer. Helical motion of the cell body enhances caulobacter crescentus motility. *Proc Natl Acad Sci U S A*, 111(31):11252–6, 2014.

[37] J. T. Locsei. Persistence of direction increases the drift velocity of run and tumble chemotaxis. *J Math Biol*, 55(1):41–60, 2007.

[38] Peter S. Lovely. Statistical measures of bacterial motility and chemotaxis. *Journal of theoretical biology*, 50(2):477 – EOA, 1975.

[39] Janine R. Maddock and Lucille Shapiro. Polar location of the chemoreceptor complex in the escherichia coli cell. *Science*, 259(5102):1717–1723, 1993.

[40] Bernardo A. Mello and Yuhai Tu. Effects of adaptation in maintaining high sensitivity over a wide range of backgrounds for escherichia coli chemotaxis. *Biophysical Journal*, 92(7):2329–2337, 2007.

[41] T. L. Min, P. J. Mears, I. Golding, and Y. R. Chemla. Chemotactic adaptation kinetics of individual escherichia coli cells. *Proc Natl Acad Sci U S A*, 109(25):9869–74, 2012.

[42] Jacque Monod, Jeffries Wyman, and Jean-Pierre Changeux. On the nature of allosteric transitions: A plausible model. *Journal of Molecular Biology*, 12(1):88–118, 1965.

[43] M. Morse, R. Colin, L. G. Wilson, and J. X. Tang. The aerotactic response of caulobacter crescentus. *Biophys J*, 110(9):2076–84, 2016.

[44] Michael Morse. *Motility of uni-flagellated bacteria: from swimming mechanics to molecular regulation*. PhD thesis, Brown University, 2016.

[45] Michael Morse, Jordan Bell, Guanglai Li, and Jay X. Tang. Flagellar motor switching in *Caulobacter Crescentus* obeys first passage time statistics. *Physical Review Letters*, 115(19):198103, 2015.

[46] J. Saragosti, V. Calvez, N. Bournaveas, B. Perthame, A. Buguin, and P. Silberzan. Directional persistence of chemotactic bacteria in a traveling concentration wave. *Proc Natl Acad Sci U S A*, 108(39):16235–40, 2011.

[47] J. Saragosti, P. Silberzan, and A. Buguin. Modeling e. coli tumbles by rotational diffusion. implications for chemotaxis. *PLoS One*, 7(4):e35412, 2012.

[48] Mark J. Schnitzer. Theory of continuum random walks and application to chemotaxis. *Physical Review E*, 48(4):2553–2568, 1993.

[49] J. E. Segall, S. M. Block, and H. C. Berg. Temporal comparisons in bacterial chemotaxis. *Proceedings of the National Academy of Sciences of the United States of America*, 83(23):8987–8991, 1986.

[50] Lee A. Segel. A theoretical study of receptor mechanisms in bacterial chemotaxis. *SIAM Journal on Applied Mathematics*, 32(3):653–665, 1977.

[51] Thomas S. Shimizu, Yuhai Tu, and Howard C. Berg. A modular gradient-sensing network for chemotaxis in escherichia coli revealed by responses to time-varying stimuli. *Molecular Systems Biology*, 6(1), 2010.

[52] M. W. Sneddon, J. R. Faeder, and T. Emonet. Efficient modeling, simulation and coarse-graining of biological complexity with nfsim. *Nat Methods*, 8(2):177–83, 2011.

[53] Kwangmin Son, Jeffrey S. Guasto, and Roman Stocker. Bacteria can exploit a flagellar buckling instability to change direction. *Nature Physics*, 9(8):494–498, 2013.

[54] V. Sourjik and H. C. Berg. Binding of the escherichia coli response regulator chey to its target measured in vivo by fluorescence resonance energy transfer. *Proc Natl Acad Sci U S A*, 99(20):12669–74, 2002.

[55] V. Sourjik and N. S. Wingreen. Responding to chemical gradients: bacterial chemotaxis. *Curr Opin Cell Biol*, 24(2):262–8, 2012.

[56] R. Stocker and J. R. Seymour. Ecology and physics of bacterial chemotaxis in the ocean. *Microbiol Mol Biol Rev*, 76(4):792–812, 2012.

[57] Roman Stocker. Reverse and flick: Hybrid locomotion in bacteria. *Proceedings of the National Academy of Sciences of the United States of America*, 108(7):2635–2636, 2011.

[58] Y. Tu. The nonequilibrium mechanism for ultrasensitivity in a biological switch: sensing by maxwell's demons. *Proc Natl Acad Sci U S A*, 105(33):11737–41, 2008.

[59] Y. Tu. Quantitative modeling of bacterial chemotaxis: signal amplification and accurate adaptation. *Annu Rev Biophys*, 42:337–59, 2013.

[60] Y. Tu and G. Grinstein. How white noise generates power-law switching in bacterial flagellar motors. *Phys Rev Lett*, 94(20):208101, 2005.

[61] Y. Tu, T. S. Shimizu, and H. C. Berg. Modeling the chemotactic response of escherichia coli to time-varying stimuli. *Proc Natl Acad Sci U S A*, 105(39):14855–60, 2008.

[62] Linda Turner, William S. Ryu, and Howard C. Berg. Real-time imaging of fluorescent flagellar filaments. *Journal of Bacteriology*, 182(10):2793–2801, 2000.

[63] Ady Vaknin and Howard C. Berg. Physical responses of bacterial chemoreceptors. *Journal of Molecular Biology*, 366(5):1416–1423, 2007.

[64] Siebe B. van Albada and Pieter Rein ten Wolde. Differential affinity and catalytic activity of chez in e. coli chemotaxis. *PLOS Computational Biology*, 5(5):e1000378, 2009.

[65] N. Vladimirov, L. Lovdok, D. Lebiedz, and V. Sourjik. Dependence of bacterial chemotaxis on gradient shape and adaptation rate. *PLoS Comput Biol*, 4(12):e1000242, 2008.

[66] L. Xie, T. Altindal, S. Chattopadhyay, and X. L. Wu. From the cover: Bacterial flagellum as a propeller and as a rudder for efficient chemotaxis. *Proc Natl Acad Sci U S A*, 108(6):2246–51, 2011.

[67] Xiangrong Xin and Hans G. Othmer. A "trimer of dimers"—based model for the chemotactic signal transduction network in bacterial chemotaxis. *Bulletin of Mathematical Biology*, 74(10):2339–2382, 2012.

[68] C. Xue and H. G. Othmer. Multiscale models of taxis-driven patterning in bacterial populations. *SIAM J Appl Math*, 70(1):133–169, 2009.

[69] Yang Yang, Jing He, Tuba Altindal, Li Xie, and Xiao-Lun Wu. A non-poissonian flagellar motor switch increases bacterial chemotactic potential. *Biophysical Journal*, 109(5):1058–1069, 2015.

[70] J. Zhuang, G. Wei, R. Wright Carlsen, M. R. Edwards, R. Marculescu, P. Bogdan, and M. Sitti. Analytical modeling and experimental characterization of chemotaxis in serratia marcescens. *Phys Rev E Stat Nonlin Soft Matter Phys*, 89(5):052704, 2014.